study is also important for the design of better dipolar recovery pulse sequences as well to refine, or to explore the limitations of, existing sequences.

Because of the nature of the dipolar interaction between like spins, analytical solutions to homonuclear DCT prove to be complex even for two-spin systems. Further understanding of DCT requires a theoretical investigation of simple two-spin systems in various experiments, which must be laid as groundwork for more complex collections of spins. In this paper, we will employ theoretical tools to explore various modes of homonuclear DCT in an unoriented solid-state system, consisting of two spin-1/2 homonuclei, both in a static powder and in the magic angle sample spinning dipolar recoupling (MASDR) experiments of USEME [58], RFDR [59], DRAMA[58] and DRAWS [57].

The main focus will be on various modes of coherence transfer as well as on the rate of coherence transfer via through space interaction, such as between directly bonded (H_{JD}, which includes both through bond and through space interactions) and approximately adjacent (H_D) ^{13}C atoms in peptides.

In MASDR experiments, chemical shift (both isotropic as well as the anisotropic) interaction can contribute to the dephasing of a coherent signal. Experimental methods for reducing the contributions of the chemical shift in MASDR have been published by the original authors in many cases, and considerations and exceptions will be discussed in the text below. In this work, we consider DCT without explicit effects from a separate chemical shift term. In Chapter 5, we will include analysis of the effects of the chemical shift to the coherence transfer process.

Theory of the Static Dipolar Hamiltonian

Consider two chemically inequivalent spin-1/2 nuclei in a sample consisting of randomly oriented polycrystallites. We assume that the dipolar coupling between the two

nuclei are non-zero. Relaxation effects are not considered in the theoretical analysis presented here, so that dephasing of the magnetization results from the loss of coherence due to the random distribution of crystallites in the powder sample and the coherent homonuclear dipolar interaction.

In the rotating frame, the total Hamiltonian consists of chemical shift, scalar coupling, and dipolar coupling terms: $H_T = H_D + H_{CS} + H_J$. We assume that an experimental situation can be created to selectively suppress the chemical shift interaction with minimal or no effect on the remaining coupling terms in the total coupling Hamiltonian. For instance, in the simplest case of a static unoriented sample, a simple spin-echo sequence in the form of a series of $\pi/2$ pulses can be utilized to refocus the chemical shifts and leave the scalar as well as the dipolar couplings unaltered (for example, see Slichter [62]). However, the effects of the residual chemical shift interaction are not considered in this study. In static solid peptides or proteins for example, H_J for homonuclear ^{13}C coupling is much smaller in magnitude than H_D and is usually neglected. However, for completeness, the contributions of scalar coupling as well as dipolar coupling to CT are included in our calculations of static samples when appropriate. Thus, we define our approximated total Hamiltonian as $H_T = H_D + H_J = H_{JD}$:

$$H_{JD} = (2D_{IS} + J)I_z S_z - (D_{IS} - J)\{I_x S_x + I_y S_y\} \quad (4\text{-}1)$$

where J is the scalar coupling constant (Hz) and D_{IS} is the dipolar coupling frequency defined as:

$$D_{IS} = \frac{\hbar \gamma_I \gamma_S}{4\pi r_{IS}^3}[1 - 3\cos^2\theta] \quad (4\text{-}2)$$

The angle θ defines the orientation of the principal axis system relative to the external magnetic field magnetic field (B_0), r_{IS} is the interatomic distance, and γ_I and γ_S

are the gyromagnetic ratios of nuclei I and S, respectively. This form of the dipolar coupling is often called the "truncated" or "secular" dipolar coupling Hamiltonian.

In an uniaxially oriented system (samples such as a single crystal or a liquid crystal or mechanically aligned bilayers or magnetically aligned bicelles), D_{IS} is dependent only on r_{IS} assuming θ is the same for all sites. In an unoriented system, D_{IS} gains an angular dependence through the distribution of θ_{IS}. Therefore, the characteristic DCT spectrum of an unoriented system is comprised of the superposition of many frequencies resulting from the summation over the spatial distribution of D_{IS}. Therefore, we expect the time- and frequency-domain components of a sample to reflect the random characteristic of the spatial anisotropy and produce a spectrum indicative of an unoriented sample; a Pake doublet powder pattern (see Figure 4-2) in the case of the frequency-domain, and therefore some kind of weighted approximate Fourier sum in the case of the time-domain signal [121].

Another interesting problem in coherence transfer through the dipolar interaction is: assuming homogenous conditions within the sample, at what rate does the coherence transfer between homonuclear spins vary for interatomic distance versus the evolution time (or mixing time under the dipolar coupling interaction)? Various experiments have been devised that have had great success in detecting DCT for a ^{13}C-^{13}C distance of less than 6 Å [69]. Therefore, it would be important to not only understand various modes of transfer of magnetization under the homonuclear dipolar coupling interaction but also the rate of transfer of magnetization in unoriented samples in MASDR experiments.

Methods

Solutions for an unoriented sample $F_D(t)$ are calculated numerically over all space in the analytical functions $F'(\theta,t)$. For each initial state $\sigma(0)$, resulting coherences evolve, each modulated by frequencies particular to the Hamiltonian under calculation in Tables

4-1 through 4-5. An initial state $\sigma(0)$ is specified for the system in the first column of the Tables and the coefficients of the product operators in the final density matrix $\sigma(t)$ are given in the subsequent columns. Tables 4-1b through 4-5b give the coherence transfer function key for Tables 4-1a through 4-5a. For example, the evolution of the initial density operator matrix $\sigma(0) = Ix$ under H_D (Table 4-1) should be read by finding Ix in the column labeled "$\sigma(0)$" and then reading across to find the operators resulting from the operation of H_D and the functions in Table 4-1b modulate those operators, in this case, it is $AIx + FIzSy - EIySz + BSz$ or, written out completely appears as equation 3-6 where α, β, γ are still defined as $\alpha = (D_{IS}/2+J)$; $\beta=(3D_{IS}/2)$; $\gamma = (J-D_{IS})$ with J being the scalar coupling and D_{IS} the dipolar coupling between spin I and spin S, both in frequency units.

For comparison, all the following simulations assume two ^{13}C nuclei at a typical glycine C_O-C_α distance of r=1.53Å corresponding to a dipolar coupling D_{CC} = 2120.7 Hz, unless otherwise noted. When included, isotropic scalar coupling is set to be 53 Hz.

Analytical calculations with all Hamiltonians were performed sequentially with any or all of the operators IzSz, IySy, and IxSx since they commute with one another. A further consequence is that these operators experience a constant of motion under H_{JD}, and so are not included in Tables 4-1 through 4-5. We assume that the initial specified state $\sigma(0)$ freely evolves under H_D.

Numerical simulations of the coherence transfer functions were performed using 250,000 crystallite orientations with assorted FORTRAN programs (see Appendix A) performing a Riemann sum over the analytical coherence transfer functions $F'(\theta,t)$ weighted by the spatial distribution probability factor $P = \sin\theta d\theta$.

Numerical simulations of unoriented samples were found to be identical to the analytical solutions for unoriented samples involving Fresnel solutions [122] first noted by Bruschweiler [121] so the accuracy of the numerical method was established for the other simulations for which no analytical solution to the spatial integral is known. FFT routines were added to provide frequency-domain data. Plots were created in Gnuplot [123] except 3-D plots, which were created in Mathematica [124] with 2-D data gathered from various FORTRAN programs (see Appendix A), referenced below.

Results and Discussion

Unoriented Sample Simulation for H_D

While it would suffice, for a simulation of randomly-oriented crystallites, to integrate the principle-axis system (PAS) spatial component of the dipolar Hamiltonian over all space, it was decided to simulate the unoriented state form of the entire laboratory-frame (LAB) transformation of the PAS form of H_D , since this would give advantages, such as the ability to include different experimental parameters, such as spinning speed and stroboscopic sample time. This transformation, which makes use of unitary transformation with the Wigner rotation matrices [60] on the high-field (truncated) Hamiltonian explicitly results in Eq. 2-16 which can also be expressed in terms of spherical harmonics.

Table 4-1 (this and next page): **(a)** Expectation values of operators evolving under the dipolar and scalar Hamiltonian. The initial states are given in the leftmost column. The evolving states are to be read across the row. For instance,
Ix evolves to AIx +BSx – EIySz + FIzSy.

(a)

s (0)↓	**Ix**	**Sx**	**Iy**	**Sy**	**Iz**	**Sz**	**2IxSy**	**2IySx**	**2IxSz**	**2IzSx**	**2IySz**	**2IzSy**
Ix	A	B									-E	F
Sx	B	A									F	-E
Iy			A	B					E	-F		
Sy			B	A					-F	E		
Iz					C	D	-G	G				
Sz					D	C	G	-G				
2IxSy					G	-G	C	D				
2IySx					-G	G	D	C				
2IxSz			-E	F					A	B		
2IzSx			F	-E					B	A		
2IySz	E	-F									A	B
2IzSy	-F	E									B	A

Table 4-1(b). Values of coefficients A-G in Table 4-1a

Function	Coefficient	Figure
A	$0.5(\cos(\alpha\pi t)+\cos(\beta\pi t))$	4-1a
B	$0.5(-\cos(\alpha\pi t)+\cos(\beta\pi t))$	4-1b
C	$0.5(1+\cos(\gamma\pi t))$	4-1c
D	$0.5(1-\cos(\gamma\pi t))$	4-1d
E	$0.5(\sin(\alpha\pi t)+\sin(\beta\pi t))$	4-1e
F	$0.5(\sin(\alpha\pi t)-\sin(\beta\pi t))$	4-1f
G	$0.5(\sin(\gamma\pi t))$	4-1g

$\alpha = (D_{IS}/2+J)$; $\beta=(3D_{IS}/2)$; $\gamma = (J-D_{IS})$

A

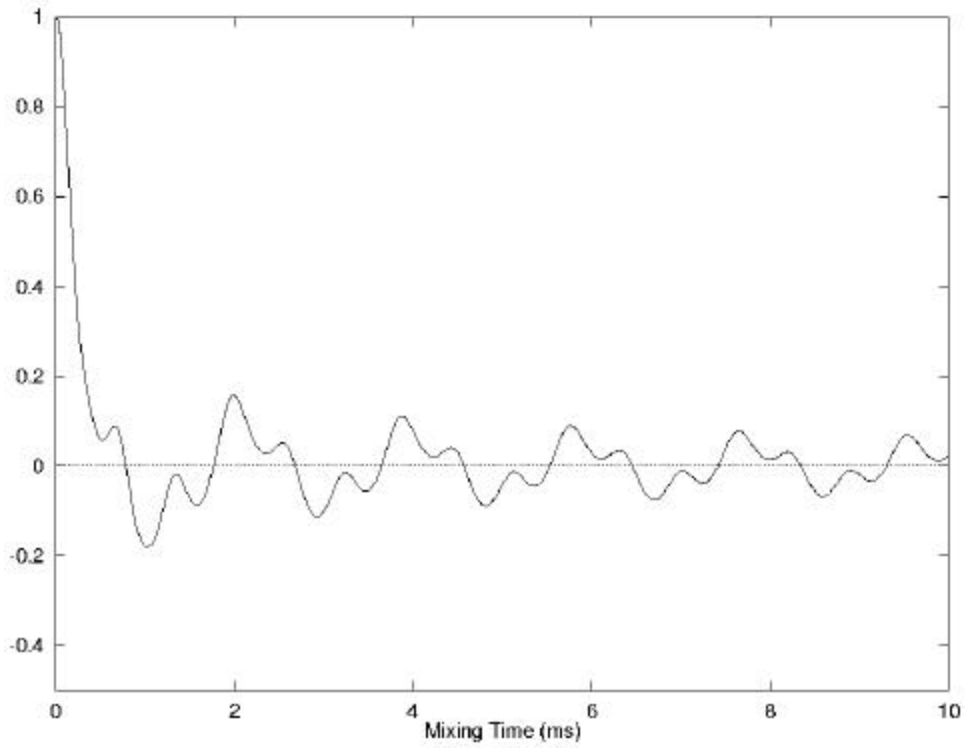

Figure 4-1 (a-g) (this and subsequent pages): Simulations of the expectation values of the operators modulated by functions A-G (Table 4-1) of an unoriented system allowed to evolve freely under H_D. The y-axis is normalized magnetization (1=100%). Simulations assumed two ^{13}C nuclei at a typical glycine C_O-C_α distance of r_{IS} = 1.53Å corresponding to a dipolar coupling D_{CC} = 2120.7 Hz.

4-1b

B

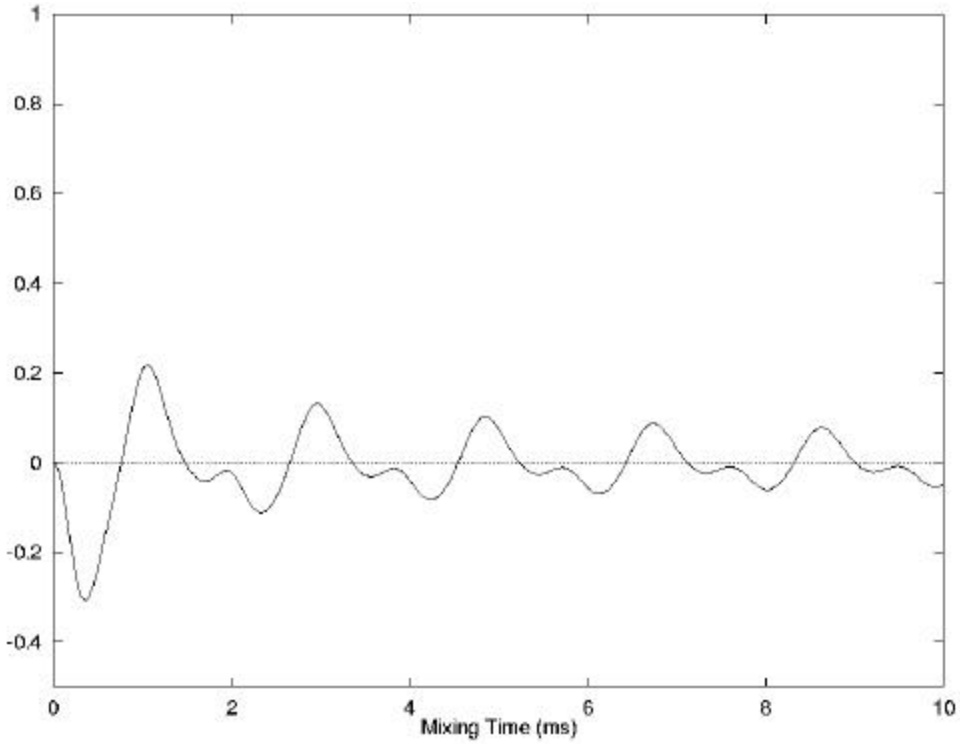
1
0.8
0.6
0.4
0.2
0
-0.2
-0.4
0
2
4
6
8
10
Mixing Time (ms)

4-1c

C

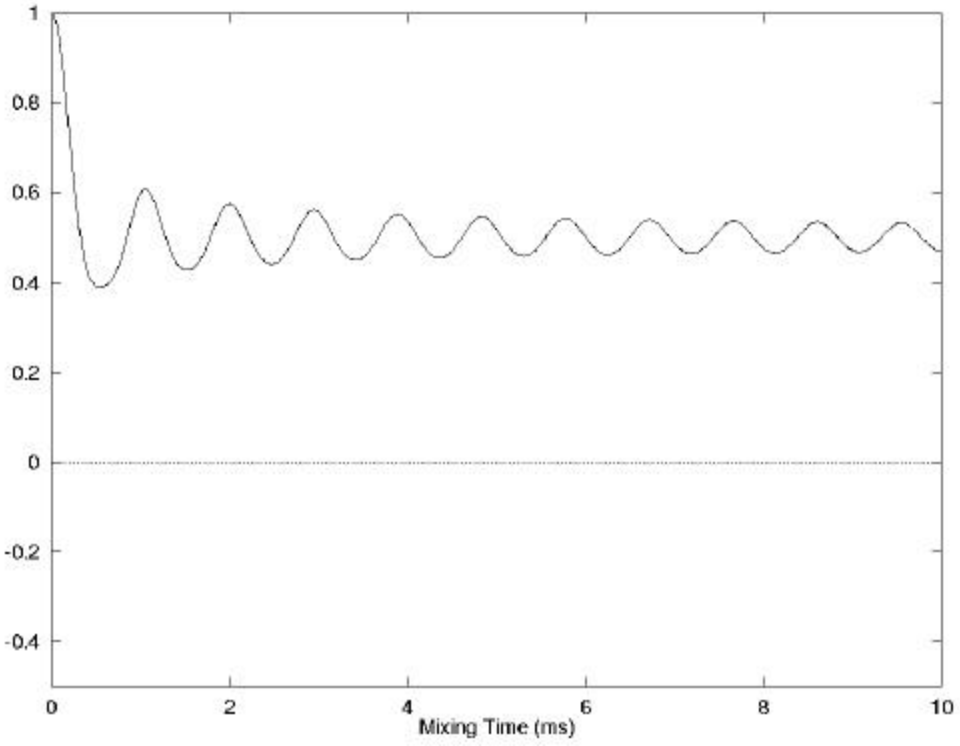
1
0.8
0.6
0.4
0.2
0
-0.2
-0.4
0
2
4
6
8
10
Mixing Time (ms)

4-1d

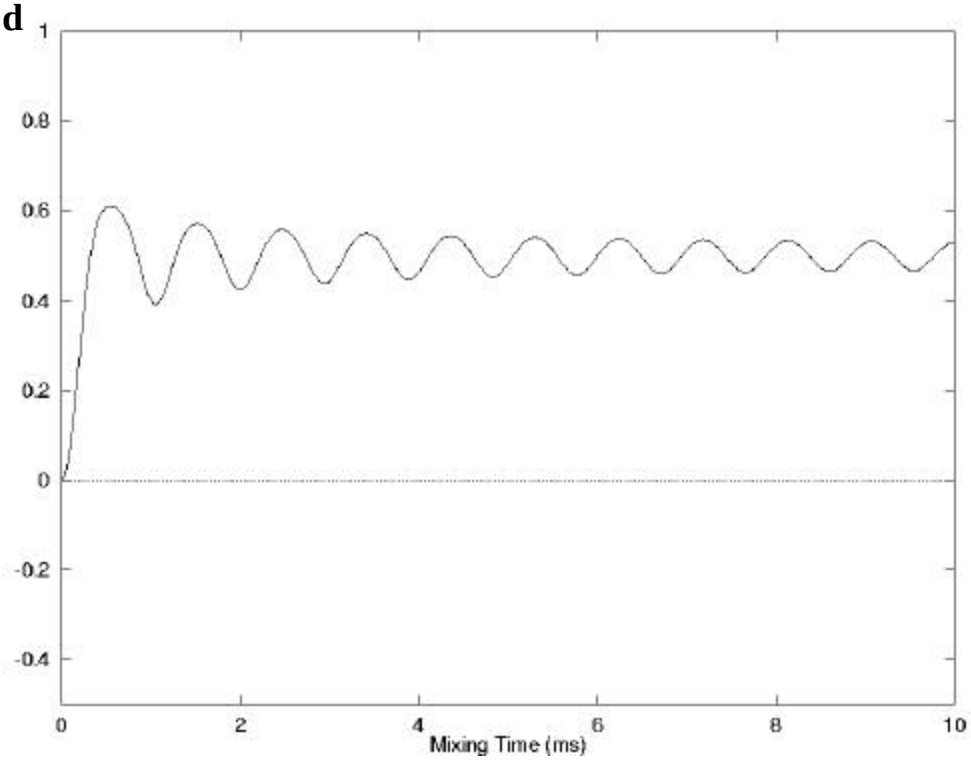
D
1
0.8
0.6
0.4
0.2
0
-0.2
-0.4
0
2
4
6
8
10
Mixing Time (ms)

4-1e

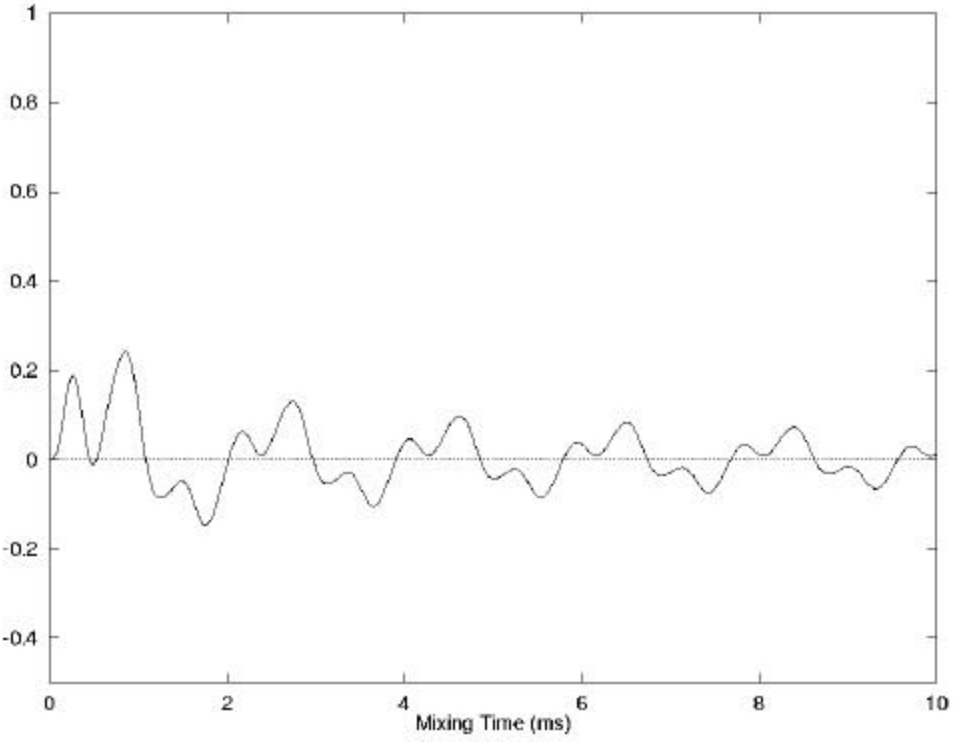
E
1
0.8
0.6
0.4
0.2
0
-0.2
-0.4
0
2
4
6
8
10
Mixing Time (ms)

4-1f

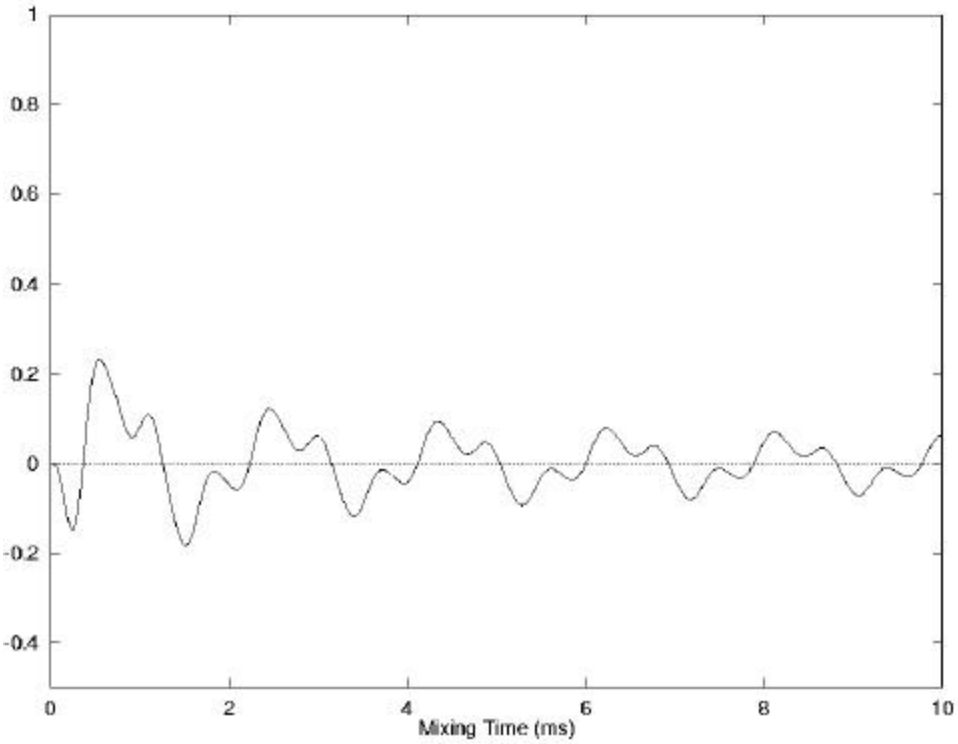
F
1
0.8
0.6
0.4
0.2
0
-0.2
-0.4
0
2
4
6
8
10
Mixing Time (ms)

4-1g

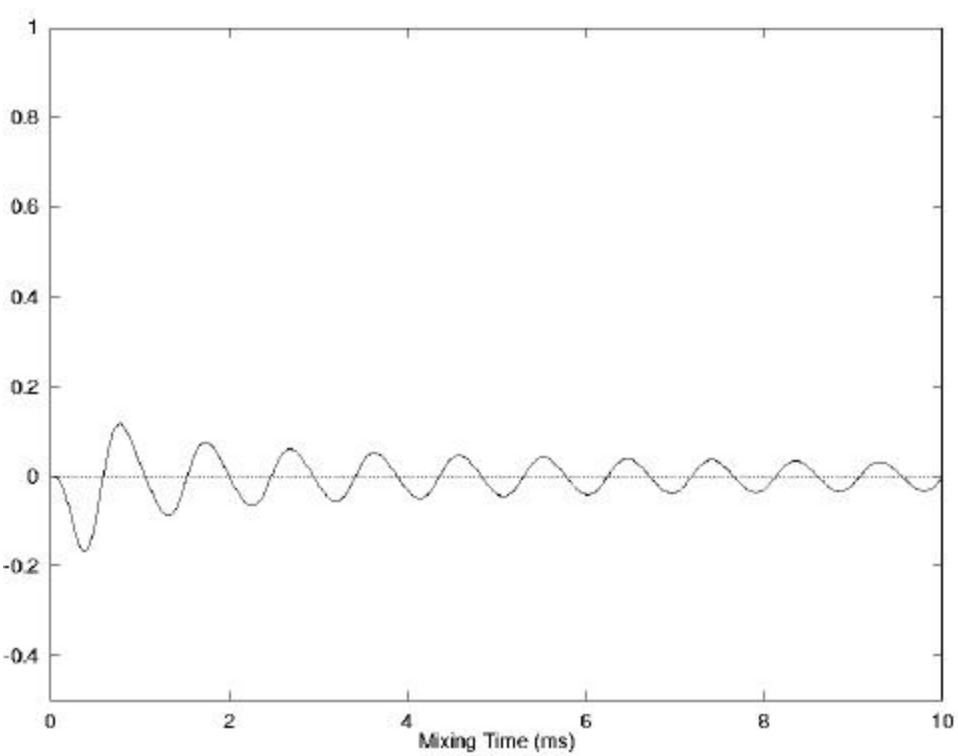
G
1
0.8
0.6
0.4
0.2
0
-0.2
-0.4
0
2
4
6
8
10
Mixing Time (ms)

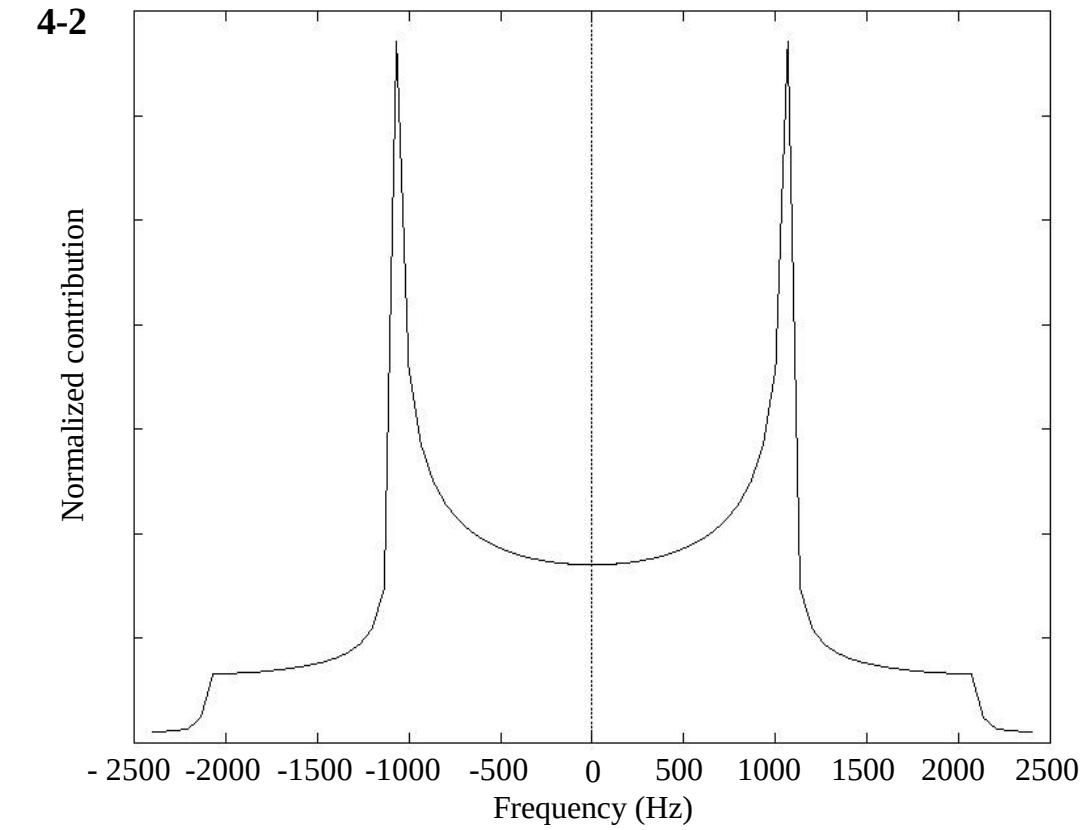

Figure 4-2: The FFT of the simulation of the time domain coherence transfer function C (Figure 4-1(c)). No window function has been used in FFT. This is the Pake doublet powder pattern spectrum due to the longitudinal DCT.

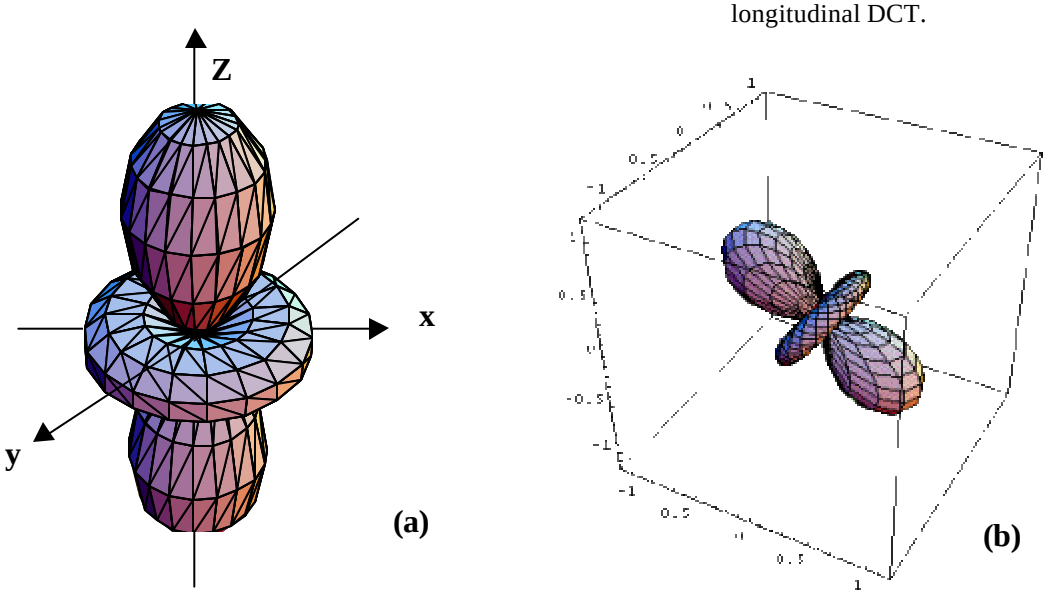

Figure 4-3 (a-b). The spherical plot representation of the spatial part of the homonuclear dipolar coupling Hamiltonian. (a) The principle-axis system representation (Eq. 4-2). (b) The spatial part of the dipolar Hamiltonian after the transformation to the laboratory frame.

The trigonometric form of D^{LAB} in Eq. 4-4 makes straightforward, typical solutions for the analytical integral of the coherence transfer functions impossible. There is no obvious analytical solution for this integration problem, although it is certainly the same form of the dipolar coupling frequency function, only spatially rotated, as can be seen in Figure 4-3(b). Despite this difficulty, an analytical solution does exist for the spatial integral of D^{PAS} while it is contained within the coherence transfer functions of A-G in Table 4-1. The term D^{PAS} (Eq. 4-2) has a simpler analytical form so can be integrated while within coherence transfer functions. This solution involves Fresnel integrals [121]. The solution is valid for D^{LAB} because we can argue that integration over all space with D^{LAB} is identical to integration of D^{PAS} over all space. In fact, by setting the angle θ_m (the angle between the PAS and the goniometer axis) in D^{LAB} Eq. 4-4 to zero returns D^{PAS} as would be expected. Unfortunately this is a special case and not true for all laboratory-frame forms of D in the various dipolar recoupling experiments, as will be seen below.

The spin parts of the coherence transfer functions for an unoriented sample based on D^{LAB} are identical as presented in Table 4-1. The evolution of the spin operators in an unoriented sample is simulated for Eqs. A-G in Table 4-1 with the program "powder.f" (given in Appendix A). For the simulations in Figure 4-1(a)-(g), the angle θ_m is set to zero to insure maximum coherence transfer. This is for the case when the goniometer frame is collinear with the external magnetic field. It is interesting to note that when the angle θ_m is instead set to the magic angle $\theta_m=57.4^o$, the third term of D^{LAB} becomes zero, but the first and second terms do not. Instead, the first and second terms "pick up" the magnitude lost by the third term, resulting in the same coherence transfer if the product of the rotor frequency and stroboscopic sampling time, $\omega_r t$, is such that the sample does not reflect equally-spaced sampling over the rotor period. It is obvious that total decoupling occurs through the stroboscopic sampling time and rotor speed arguments within the cosine terms, as simply placing the PAS axis at the magic angle to the laboratory frame is

not enough to isotropically average the anisotropic dipolar coupling interactions, but stroboscopic sampling and spinning is also necessary.

The magnitude of the terms A-G are plotted respectively in Figure 4-1(a)-(g), as a function of the mixing time under the Hamiltonian H_D. The simulations show the time-domain behavior under the dipolar coupling Hamiltonian (Eq. 4-4). For example, the magnitude axis in Figure 4-1(a) corresponds to the amount of normalized magnetization that remains in the source (the I nuclei) when the x magnetization of the I nuclei is selected for coherence transfer under the coupling Hamiltonian H_D. Similarly, Figure 4-1(b) represents the expectation value of the Sx operator as magnetization is transferred from the I to the S nuclei when x magnetization of the I nuclei is selected for coherence transfer under the coupling Hamiltonian H_D.

It can be immediately seen from Figure 4-1 that longitudinal and transverse coherence transfer (for example $\sigma(0)=Iz$ or $\sigma(0)=Ix$) is markedly different in character. In previous work ([40] and Chapter 3) we have referred to this as “cylindrical mixing”. The unique pattern of evolution in the numerical results for the spatially-averaged functions in Table 4-1(b) could theoretically lend themselves to detecting internuclear distances based on the magnitude and/or phase of dipolar coherence transfer as a function of mixing time. Recent work has shown the effects of cylindrical mixing on three spin systems [125].

The DCT characteristics of functions C and D in Figures 4-1(c) and (d) (corresponding to longitudinal coherence transfer) arise because of the identical frequency components of the transverse IxSx and IySy operators. The initial state $\sigma(0) = Iz$ is normalized to 100% magnetization at t = 0 (Figure 4-4(a)). The Iz and Sz operators form a coupled coherent pair. Since Iz is an operator representing the self-magnetization of the I spins, the expectation value for Table 4-1’s Eq. C as well as the self-magnetization for the second spin in Eq. D oscillates around an average 50%, as expected for two identical coherently coupled systems sharing a normalized magnetization (100%)

at t = 0. The particular shape of the graphs in Figures 4-1(c) and (d) arise because of the modulation by the probability factor $\sin\theta d\theta$.

The expectation value of the zero-quantum coherence operator (IxSy - IySx) that appears when $\sigma(0) = Iz$ evolves under Eq. G of Table 4-1, whose maximum value is very much smaller than the population operators and reaches its maximums at the time of the common nodes between the two spins.

The Fourier transform of the time-domain of function C (Figure 4-1(c) results in the typical Pake doublet shape (Figure 4-2) with the frequencies between the two zero-pole peaks of a spherically distribution of crystallites spanning a frequency distance corresponding to D_{IS}†. The shape of the time-domain functions for DCT arises from the same effect that causes the shape of the Pake doublet, which is the behavior of the trigonometric transfer functions on the integral over the sphere around $\theta = 0$ radians.

The "DCT rise time" can be characterized as the time at which one spin has transferred the maximum magnetization to the second spin. This is best observed in the expectation value of the operators. The initial peak for DCT in unoriented samples (Eq. D) overshoots the 50% transfer, making its evolution easy to follow Figure 4-8(a) traces this first maximum DCT peak, which is at the crest of the "rise time." The best-fit equation is $r = 2.67\ t^{1/3}$, where r is the internuclear distance and t is the mixing time, with an R-squared fit of 1. Therefore, the maximum rate of coherence transfer, υ, in an unoriented sample is $u = \frac{dr}{dt} = 0.89t^{-\frac{2}{3}}$, shown in Figure 4-8(b). Note the sharp drop-off, where the initial velocity is well below 1Å/ms by 1ms mixing time. The implication of Figure 4-8 indicate that in powders, the rate of coherence transfer in a sample under H_D cannot be predicted by the dipolar coupling constant alone, but instead the summed coherence transfer behavior must be accounted for when considering rise times and maximum coherence transfer rates. This equation indicates, for example, that under

† Usually the frequency span of a Pake doublet in a homonuclear dipolar-coupled system is 3/2 D when calculations include the transitions from the dipolar Hamiltoinan with the Zeeman Hamiltonian. However, this doublet will be simply span the domain D as we are not including the Zeeman interaction in this example, but merely a representative FFT of the coherence transfer functions.

optimal conditions in a completely unoriented sample, it would take a total of 1.41 ms to transfer maximum coherence to a site 3 Å away.

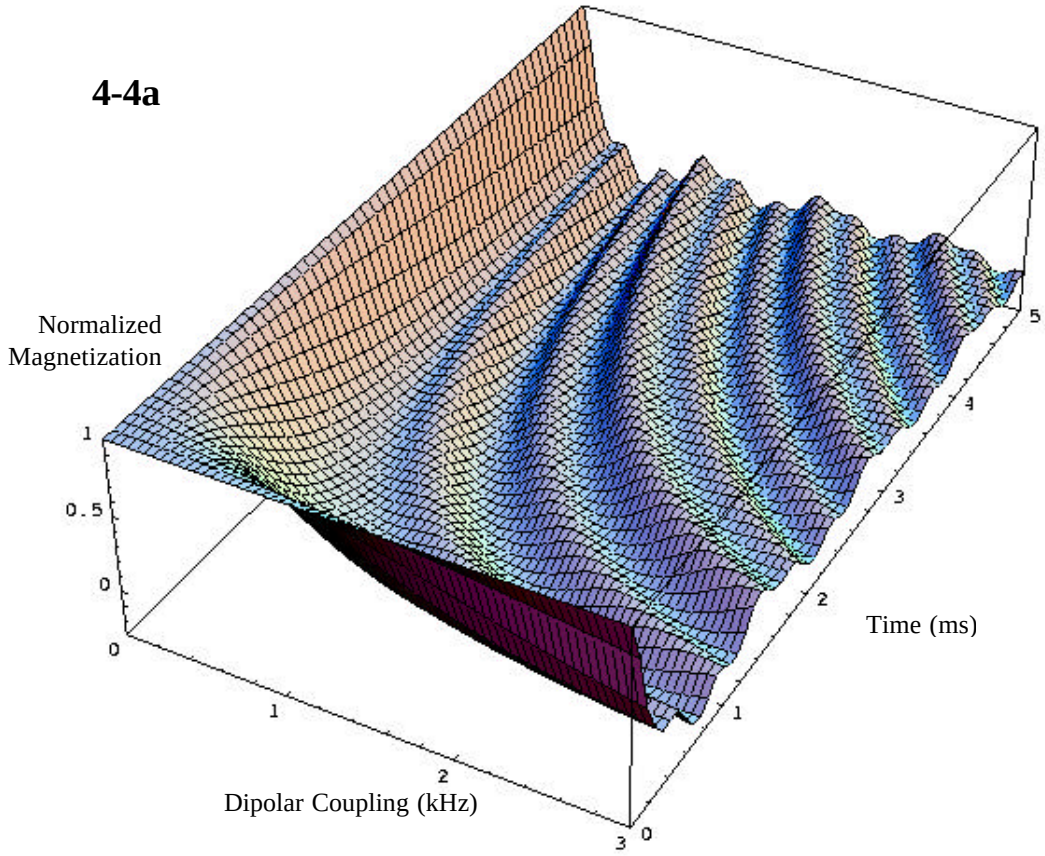

Figure 4-4 (a-d) (this and next page). (a) Three-dimensional plot showing the dependence of the expectation value of Function A in Table 4-1, representing the transverse self-magnetization retained by the first spin through DCT in an unoriented two-spin 13C homonuclear system, for example when $\sigma(0) = I_x$. Two-dimensional slices (b), (c), and (d) are taken from the three-dimensional plot in (a) for the evolution times 2, 5, and 10ms respectively, shown for J=0 (solid lines) and J=53 Hz (dashed lines). normalized magnetization

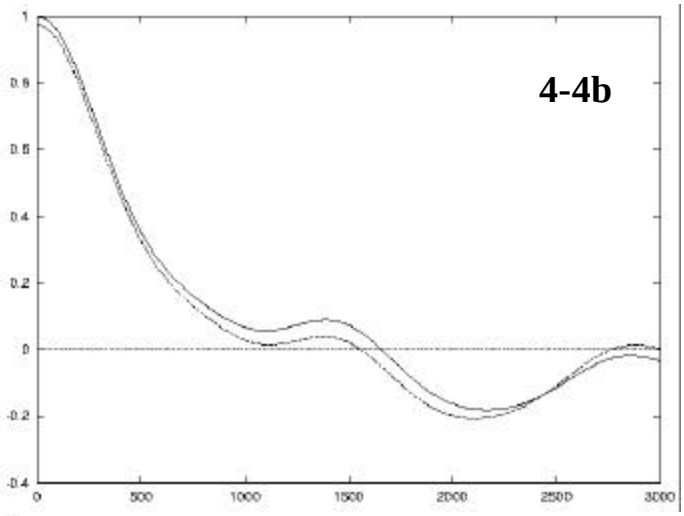
4-4b

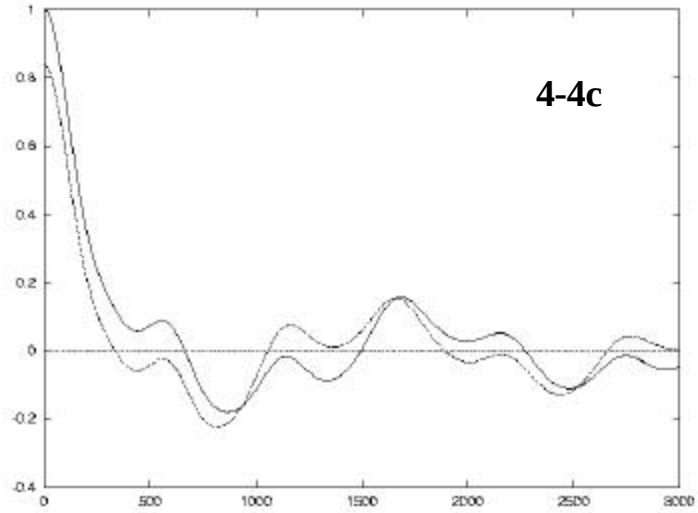
4-4c

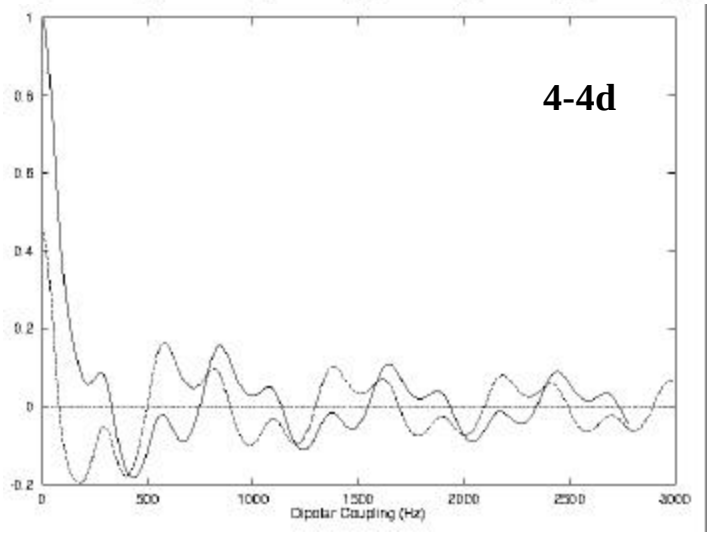
4-4d
Dipolar Coupling (Hz)

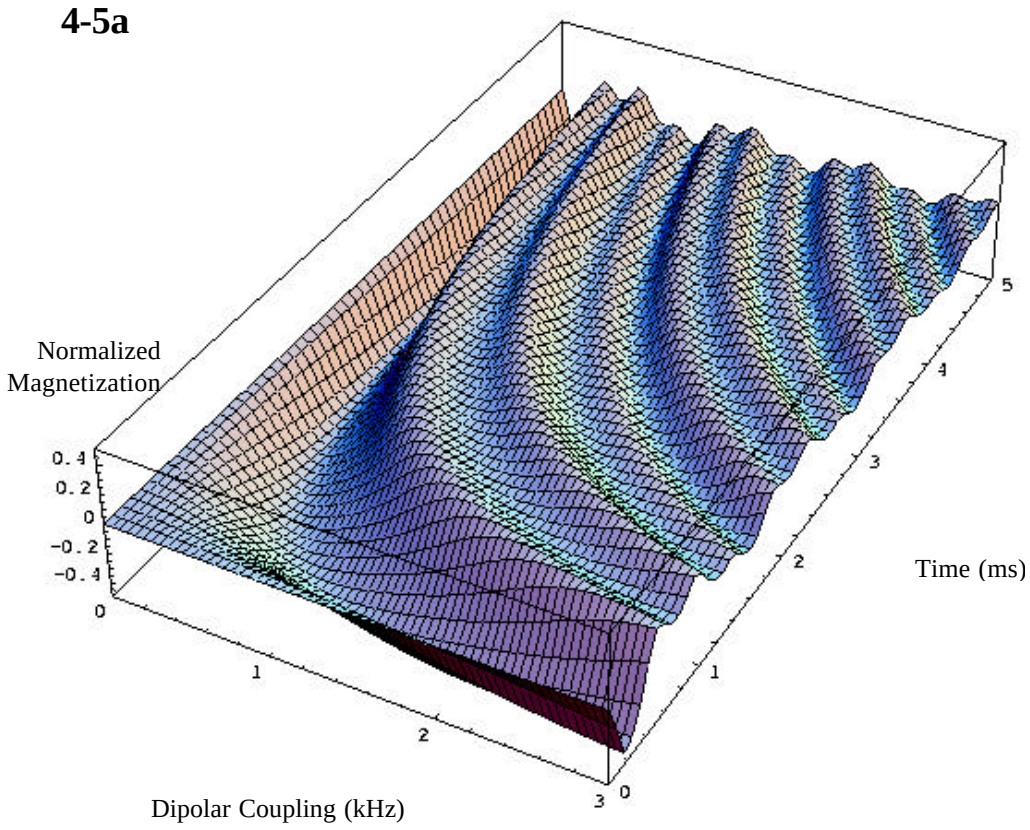

Figure 4-5 (a-d) (this and following page). (a) Three-dimensional plot showing the dependence of the expectation value of Function B in Table 4-1, representing the transverse magnetization transferred to the second spin through DCT in an unoriented two-spin 13C homonuclear system, for example when $\sigma(0) = I_x$. Two-dimensional slices (b), (c), and (d) are taken from the three-dimensional plot in (a) for the evolution times 2, 5, and 10ms respectively, shown for J=0 (solid lines) and J=53 Hz (dashed lines). normalized magnetization

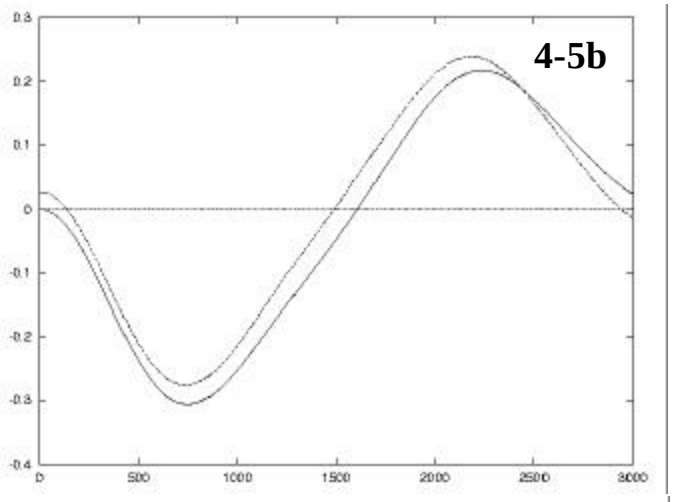
4-5b

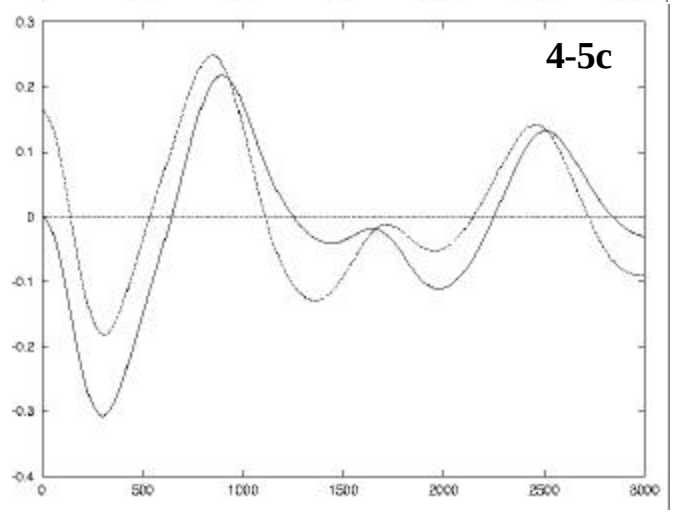
4-5c

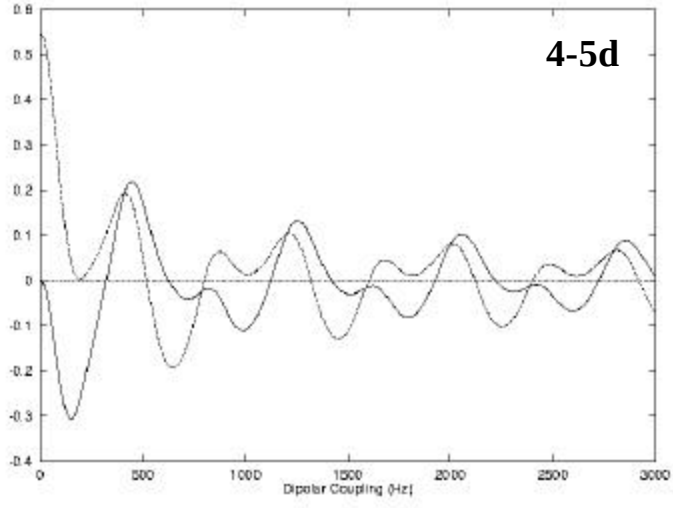
4-5d
Dipolar Coupling (Hz)

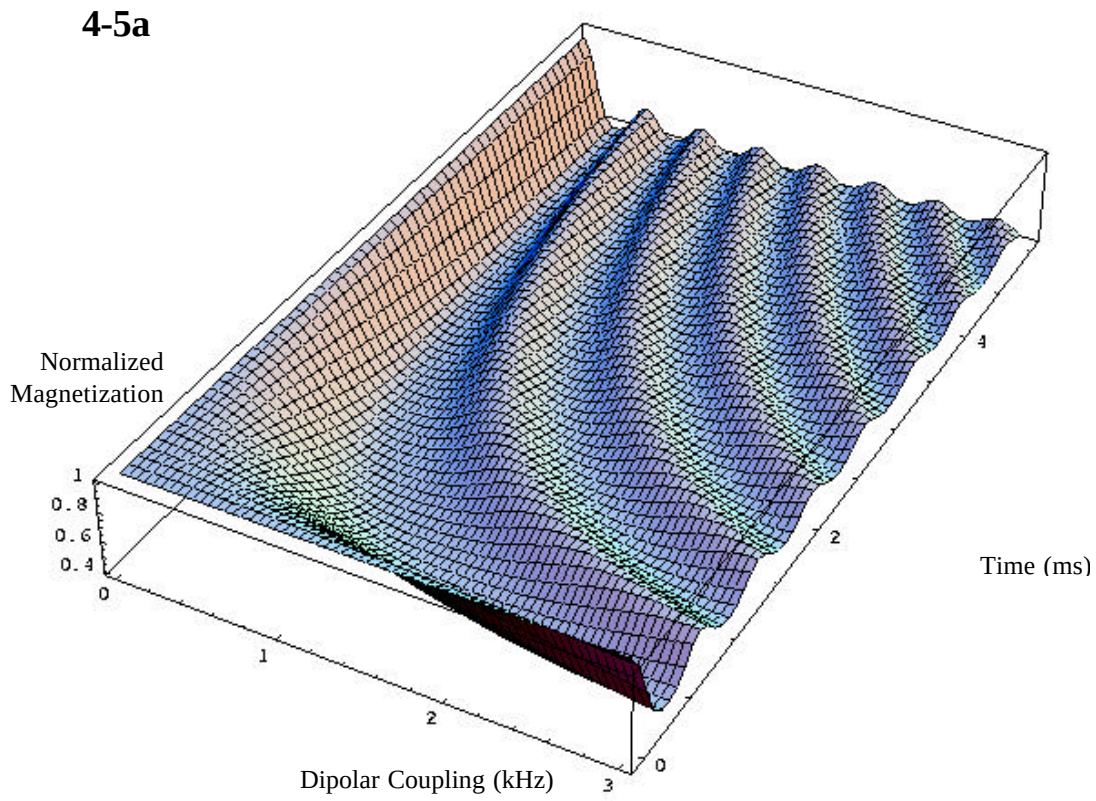

Figure 4-6 (a-d) (this and following page). (a) Three-dimensional plot showing the dependence of the expectation value of Function C in Table 4-1, representing the longitudinal self-magnetization retained by the first spin through DCT an unoriented two-spin 13C homonuclear system, for example when $\sigma(0) = I_z$. Two-dimensional slices (b), (c), and (d) are taken from the three-dimensional plot in (a) for the evolution times 2, 5, and 10ms respectively, shown for J=0 (solid lines) and J=53 Hz (dashed lines). normalized magnetization

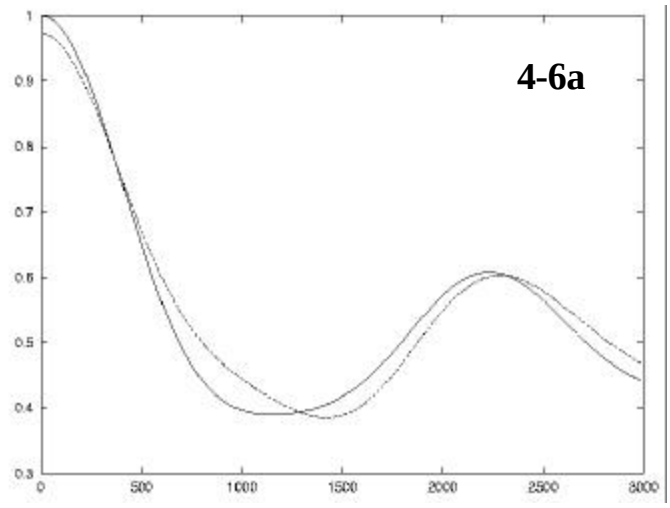
4-6a

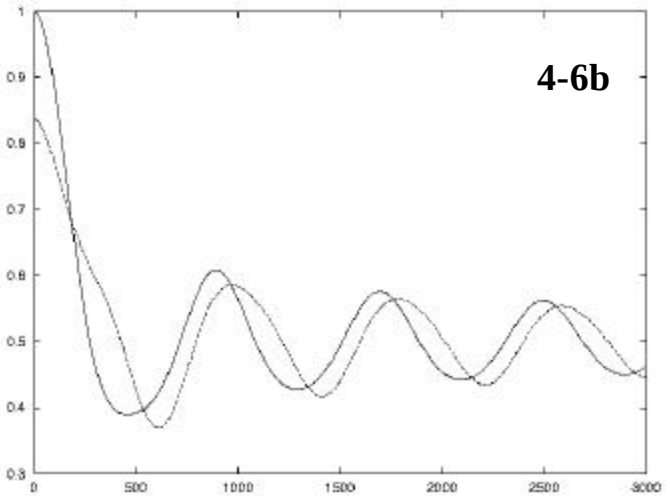
4-6b

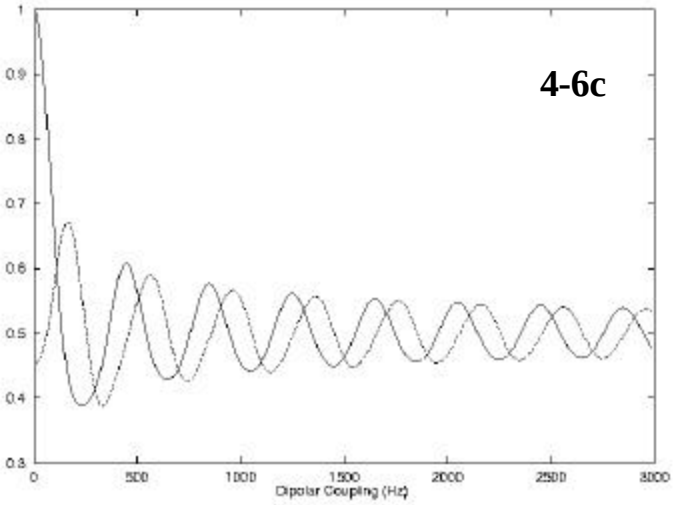
4-6c
Dipolar Coupling (Hz)

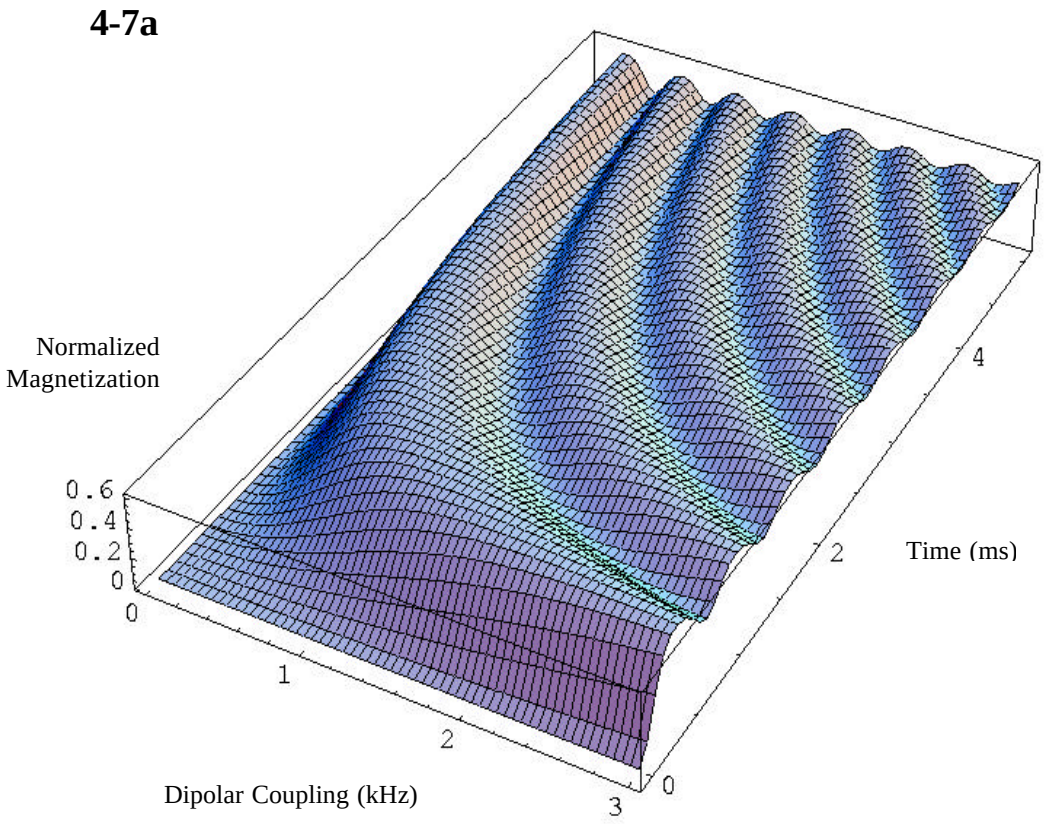

Figure 4-7 (a-d) (this and following page). (a) Three-dimensional plot showing the dependence of the expectation value of Function D in Table 4-1, representing the longitudinal magnetization transferred to the second spin through DCT in an unoriented two-spin ^{13}C homonuclear system, for example when $\sigma(0) = Iz$ Two-dimensional slices (b), (c), and (d) are taken from the three-dimensional plot in (a) for the evolution times 2, 5, and 10ms respectively, shown for J=0 (solid lines) and J=53 Hz (dashed lines). normalized magnetization

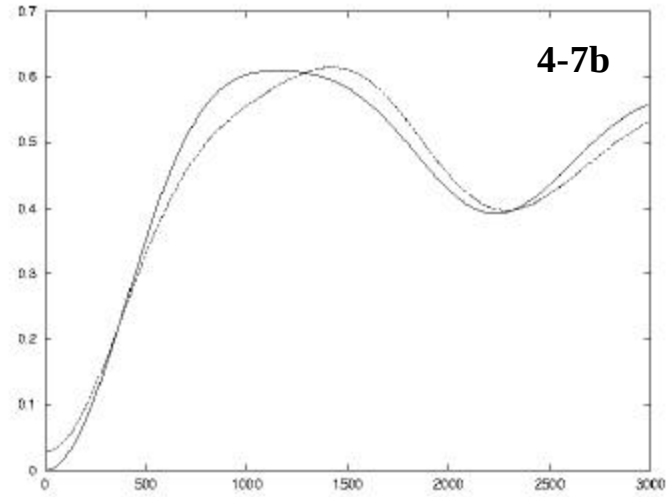
4-7b
0.7
0.6
0.5
0.4
0.3
0.2
0.1
0
0
500
1000
1500
2000
2500
3000

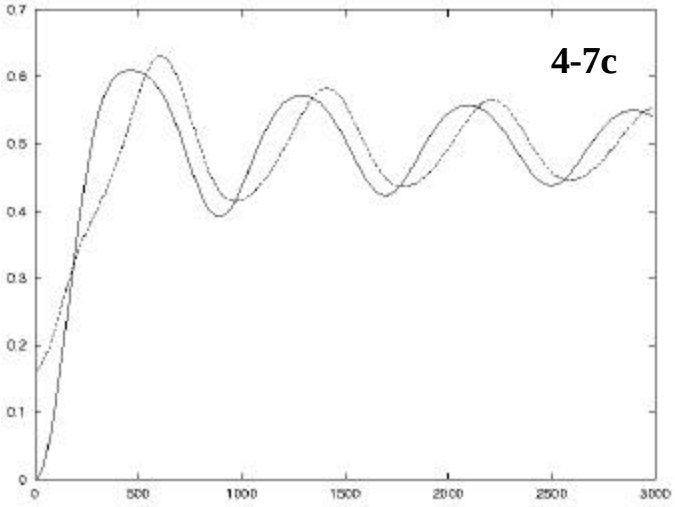
4-7c
0.7
0.6
0.5
0.4
0.3
0.2
0.1
0
0
500
1000
1500
2000
2500
3000

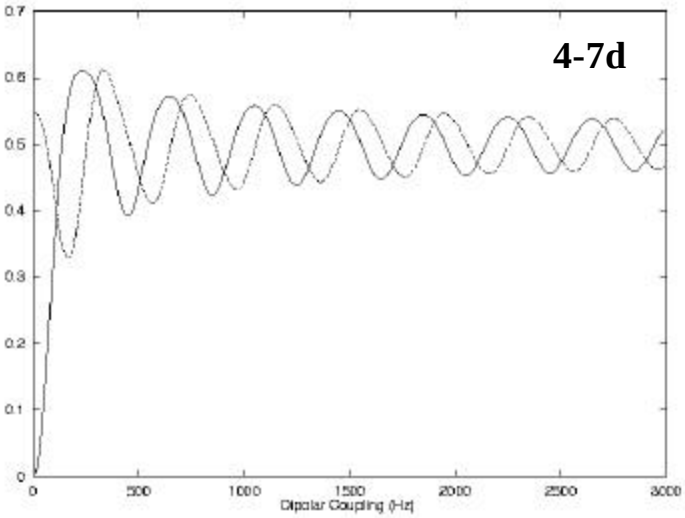
4-7d
0.7
0.6
0.5
0.4
0.3
0.2
0.1
0
0
500
1000
1500
2000
2500
3000
Dipolar Coupling (Hz)

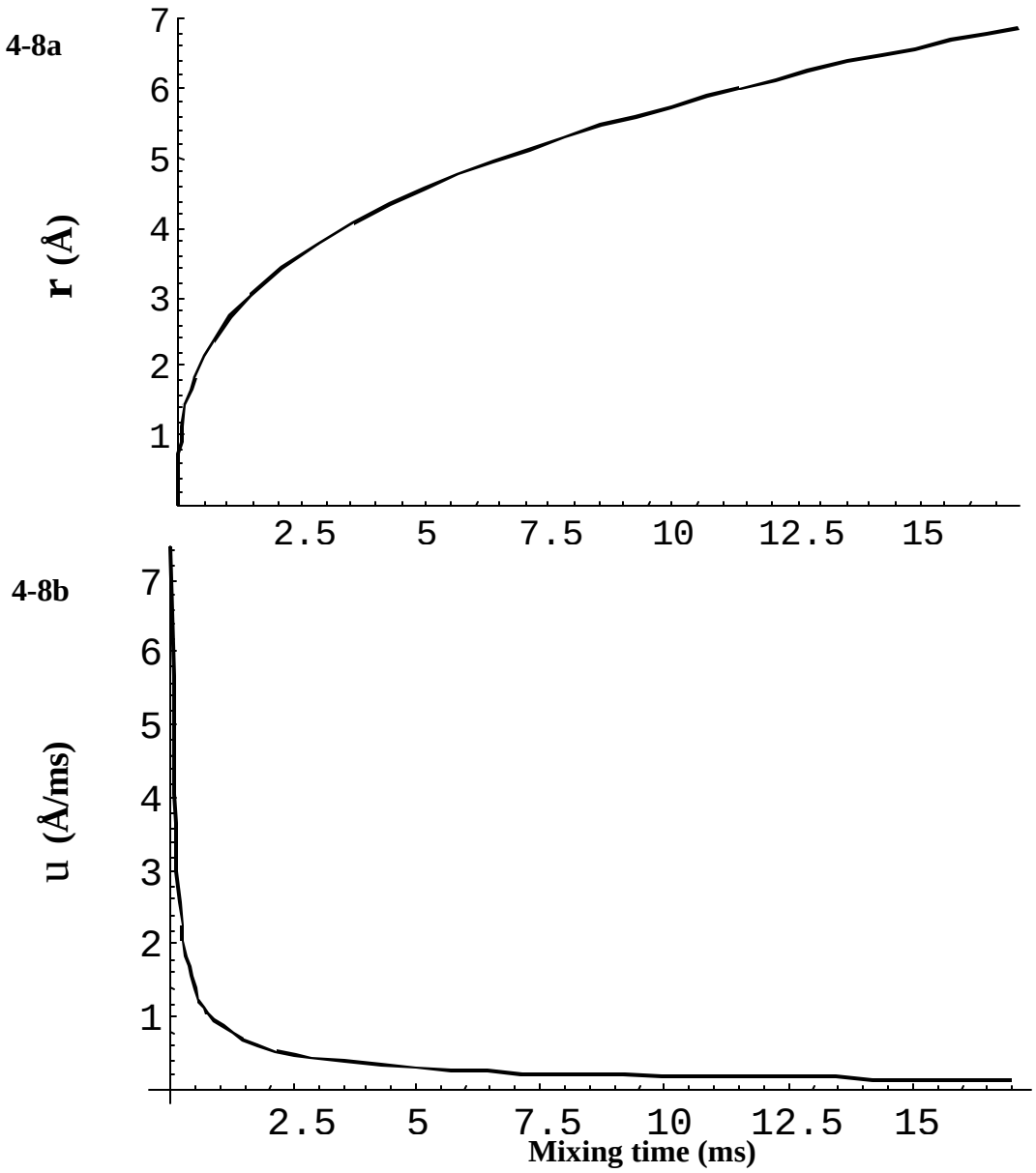

Figure 4-8 (a-b): (a) The trace of maximum coherence diffusion peak of Function D in Table 4-1, representing the maximum transferred longitudinal magnetization to the second spin in an unoriented two-spin ^{13}C homonuclear system, for example when $\sigma(0) = Iz$. $r = 2.67\ t^{1/3}$ Scalar coupling was assumed to be zero. (b) The rate of coherence transfer , υ, versus mixing time (Å/ms). $\upsilon = 0.89\ t^{-2/3}$

The DRAMA Experiment

The DRAMA experiment [56] is one of the simplest of MASDR experiments. The uncorrected form of the DRAMA pulse sequence (Figure 4-9) is performed over the period of one rotor rotation. A single 90^{o}_{x} pulse brings the equilibrium Iz magnetization to –Iy, during which time mixing can occur between I and S nuclei within the space of the rotor period. A 90^{o}_{-x} pulse restores the Iz magnetization, and then additional pulses are supplied to observe the magnetization of the system. The DRAMA pulse sequence prevents the dipole-dipole coupling from averaging to zero the average Hamiltonian over one pulse sequence:

$$\tilde{H}_{DRAMA} = \frac{-\hbar ?^{2}}{pr^{3}} Y_{IS}[IzSz - IySy] \qquad (4\text{-}5)$$

with the spatial part of the DRAMA Hamiltonian being a special rotated form of the second-rank spherical harmonics Y_{2m} , explicitly:

$$Y_{IS} = \frac{\sqrt{2}}{2}\sin 2q \cos j \sin(\frac{tn_{r}}{2}) + \frac{1}{4}\sin^{2} q \cos 2j \sin tn_{r} \qquad (4\text{-}6)$$

where τ is the period between the pulses in radian-seconds (Figure 4-9) and ν_r is the rotor frequency in Hz.

The form of the spin part of the Hamiltonian (**IzSz – IySy**) generates strong coupling DCT only in the operator subspace spanned by Ix, IySz, IzSy, and Sx. As we saw in Chapter 2, strong-coupling DCT depends on coherence transfer through two of the three operators (IxSx, IySy, IzSz) that do not commute with $\sigma(0)$. Therefore, weak-coupling-like DCT or no DCT occurs for all other operators, which commute with one or both of IzSz or IySy. In Figure 4-10, the expectation values due to the only three effective coherence transfer functions A, B, and C from Table 4-2 are shown. The

coherence transfer function "A" represents, for example, the self-magnetization of the I-spins when $\sigma(0)=I_x$. This particular behavior can be compared to the function C in the static, unoriented sample (Figure 4-1(c)). Likewise, curve B in Figure 4-10 represents the transferred magnetization to the second spin over the DRAMA irradiation time with H_{DRAMA}. The two coherence transfer functions, A and B, form a coupled pair. However, unlike the static unoriented sample case, there is no zero-quantum operator or its analog in DRAMA with this coupled pair. The other group members, I_YS_Z and I_ZS_Y, are modulated by a coherence transfer function E (Table 4-2) in which H_{DRAMA} averages to zero over space. In fact, both function E and function D average to zero, because they are odd functions of mixing time, while A, B and C are even functions. partially-recovered strong coupling that transfers coherence along the transverse direction.

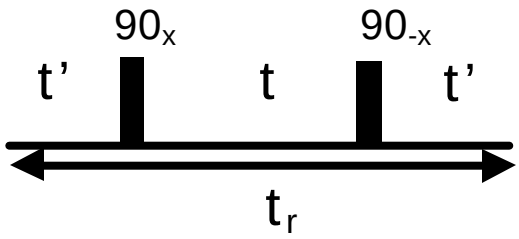

Figure 4-9: The DRAMA pulse sequence.

The variation in the efficacy of DRAMA DCT is not only due to the initial state $\sigma(0)$, but is also a function of the ratio of the inner mixing time to the rotor period (Figure 4-9). A FORTRAN program, tdrama.f (Appendix A), was written to simulate the coherence transfer over various values of τ/τ_r and the results are plotted in Figure 4-11. It can be immediately noted that the value of τ/τ_r introduces a new variable to control DCT in DRAMA. The significance of varying τ/τ_r is apparent when the effects of the variation are seen on the spatial component Y_{IS} of the DRAMA Hamiltonian. Figure 4-12 depicts the spherical form of the spatial component depending on the ratio τ/τ_r. The variation in the DCT behavior based on the ratio value can be better understood as a combined frequency resulting from a Riemann sum over the surface values of the lobed graphs.

Table 4-2 (this and next page): (a) Expectation values of operators evolving under the DRAMA coupling Hamiltonians. The initial states are given down the leftmost column. The evolving states are to be read across the row. For instance, Ix evolves to AIx – BSx – E(IySz + IzSy).

s **(0)** ↓	**Ix**	**Sx**	**Iy**	**Sy**	**Iz**	**Sz**	**2IxSy**	**2IySx**	**2IxSz**	**2IzSx**	**2IySz**	**2IzSy**
Ix	A	-B									-E	-E
Sx	-B	A									-E	-E
Iy			C						D			
Sy				C						D		
Iz					C		D					
Sz						C		D				
2IxSy					-D		C					
2IySx						-D		C				
2IxSz			-D						C			
2IzSx				-D						C		
2IySz	E	E									A	-B
2IzSy	E	E									-B	A

Table 4-2(b): Coefficients of the spin operators generated due to the evolution under H_{DRAMA}

Function	Form	Figure
A	$\cos^2(0.5at)$	4-10, curve A
B	$\sin^2(0.5at)$	4-10, curve B
C	$\cos(at/2)$	4-10, curve C
D	$\sin(at/2)$	-
E	$0.5\sin(at)$	-

$$a = \frac{3d_{IS}}{\sqrt{6}} Y_{IS}$$

The total average Hamiltonian for DRAMA is anisotropic, corresponding to a term in Y_{IS} which reaches a maximum magnitude at $\tau/\tau_r = 0.5$ and then follow a mirrored reduction (where, for example, in Figure 4-12, a value approaching $\tau/\tau_r=1$ will find the opposite lobes shrinking into the rotated dz^2 shape).

But what effect does varying τ/τ_r have on the velocity of DCT in DRAMA? To determine the rate of coherence transfer, simulations using the ddrama.f and pdrama.f (Appendix A) programs were run, with the results plotted in Figure 4-13. The graph follows that maximum for the three independent variables of τ/τ_r, distance between nuclei, and experimental time. This plot implicitly represents the maximum transfer amplitude for Function B in Table 4-2, such as found at ~1.7 milliseconds for curve B in Figure 4-10. It should be noted that the magnitude of maximum coherence transfer varies between 52% and 63% of normalized magnetization because of the effects of τ/τ_r on the DCT behavior, but in all cases the program followed the maximum peak for all values of τ/τ_r . This can be interpreted as the possible DCT velocities based on the ratio τ/τ_r set in the DRAMA pulse sequence for the transferred transverse magnetization in a homonuclear ^{13}C pair.

It is clear that the rate of DCT can be controlled by varying τ/τ_r For example, the first maximum coherence peak in DRAMA will arrive at an internuclear distance of 2 angstroms in 3 milliseconds using a τ/τ_r ratio of 0.5. It is also obvious from the graph that this rate of DCT is not constant, because the internuclear distance axis has a time-dependent curvature, while the τ/τ_r axis varies with internuclear distance . Like the unoriented sample DCT rate curve presented in Figure 4-8, DRAMA also has a predictable pattern of DCT behavior that also depends on τ/τ_r. The curvature of the rate transfer function increases with increasing ratio.

It is also important to consider the experimental mixing time that is implicit to the pulse sequence. Because the DRAMA experiment transfers magnetization transversely, it is sensitive to T2 relaxation. Figure 4-11 depicts the cross-section along the ratio axis for various DRAMA experimental times.. In this example of a system where r = 1.53Å, the DCT is still fairly small at 0.75 ms, less than 40%, as can be seen in Figure 4-11, and for systems with larger r, the DCT would be appreciably less for the same experimental time. Repeating sequences are therefore used during experiment. For a system with a τ/τ_r ratio of 0.5, we would expect that two DRAMA experimental sequences would have to be used to transfer a good percentage of the magnetization between the two nuclei; in this case, 1.2 ms transfers nearly 52 percent of the magnetization between the two sites.

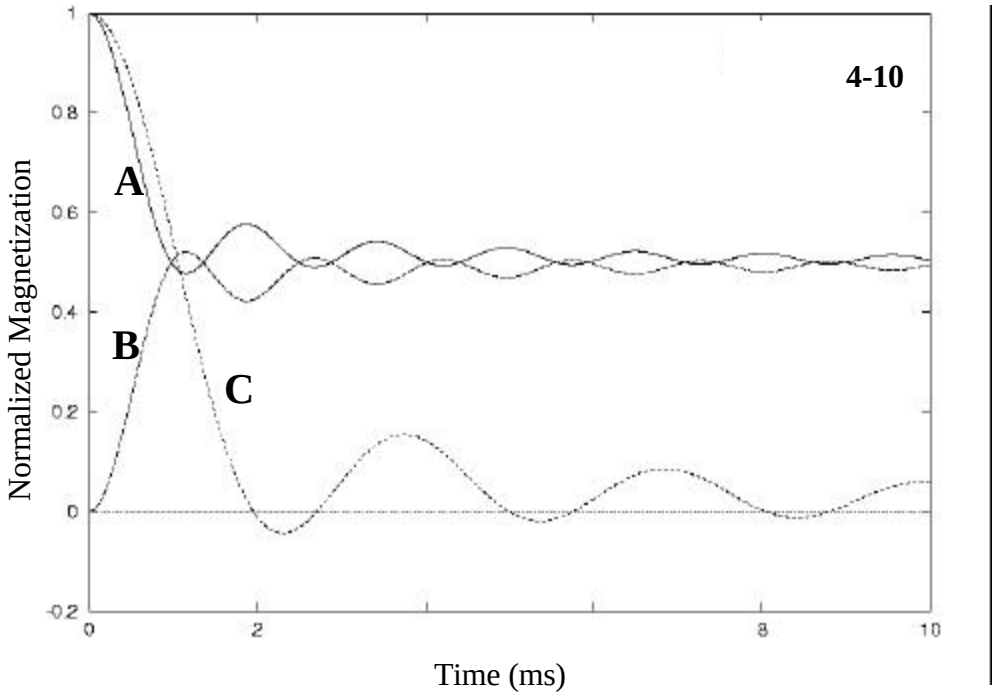

Figure 4-10: Powder-averaged expectation values for operators evolving with coefficients A, B, and C from Table 4-2 for $\tau/\tau_r = 0.50$ for a ^{13}C homonuclear system as a function of DRAMA experimental time, r_{IS}=1.53Å.

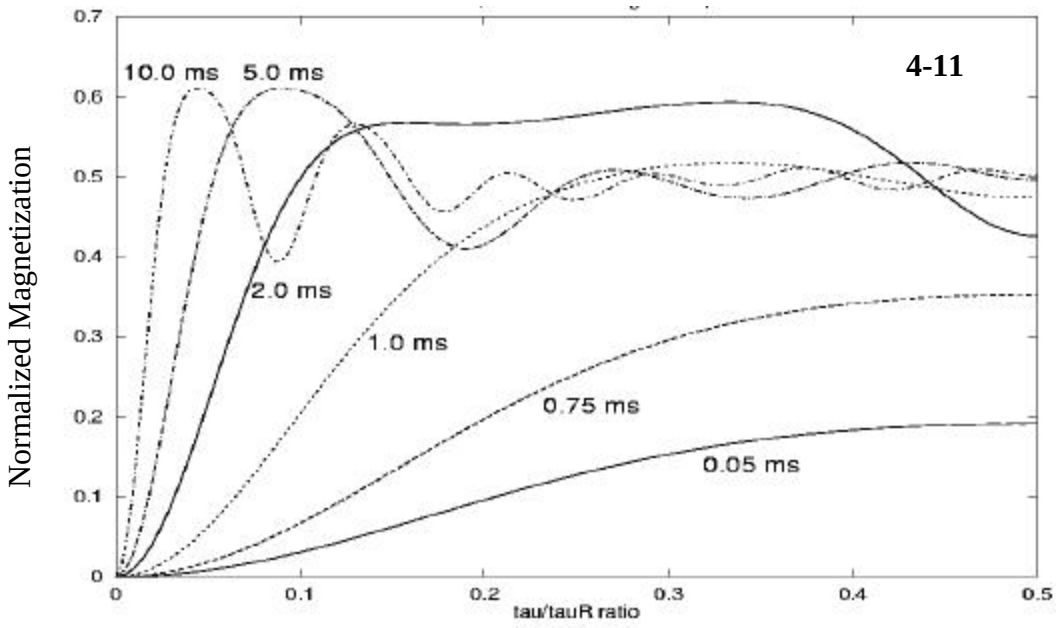

Figure 4-11: Dependence of DCT magnitude on the ratio of τ/τ_r for a series of experimental times for the powder-averaged expectation value <Sx> corresponding to the DCT coefficient B in Table 4-2. Continuation of this graph to $\tau/\tau_r = 1$ causes the curves to mirror around $\tau/\tau_r = 0.5$.

It is obvious from Figure 4-11 that multiple DRAMA sequences are needed to increase the effective inner mixing time τ in order to transfer an appreciable amount of magnetization along biologically important internuclear distances where the loss of transverse coherence over greater DRAMA experiment time is due to non-zero offsets or other inhomogenities. We will explore the situation of non-zero chemical shift in the next chapter.

It can be expected that a series of DRAMA pulse groups will accommodate DCT for a wider range of distances, but with three independent parameters (distance, τ/τ_r, and DRAMA experimental time) it is necessary to optimize the experiments for each particular system. In particular, it may be possible to separate out DCT in individual pairs of ^{13}C nuclei through optimizing experimental parameters for particular internuclear distances.

For instance, it seems possible to optimize the ratio of τ/τ_r according to the sample system . According to Figure 4-13, the optimal ratio of τ/τ_r is 0.2 for greater than 50% magnetization transfer over a 5 ms experimental time for a pair of ^{13}C nuclei separated by 2Å. Since DRAMA is subject to the loss of coherence due to T2 processes, the experiment would be better optimized by decreasing the experimental time. It is clear that by changing the ratio of τ/τ_r to 0.5 the experimental time can be decreased while still transferring the same amount of magnetization between sites of identical distance. Conversely, there may be some experiments that seek to increase the experimental time to distinguish internuclear distances between sites, which can be done by decreasing the value of τ/τ_r. The maximum DCT for a DRAMA experiment seems to be when τ/τ_r=0.5. The trace of the maximum magnetization DCT over a range of distances for DRAMA as a function of experimental time when τ/τ_r=0.5 is given in Figure 4-14(a), corresponding to an equation of $r = 1.41\ t^{1/3}$.

The maximum rate of coherence transfer υ_{DRAMA} in given in Figure 4-14(b) for τ/τ_r=0.5. Its value, $\upsilon_{DRAMA} = 0.47\ t^{-2/3}$, is 52% that of the rate of transfer of the full

dipolar powder-averaged Hamiltonian. This low rate allows T_2 processes to be more influential during the lifetime of DCT in DRAMA. On the other hand, the slow DCT rate may also prove itself useful in resolving internuclear distances for several pairs of homonuclei with differing internuclear distances, based on the experimental time of maximum DCT (*vide infra*) in appropriately-designed DRAMA experiments with little to no chemical shift offset.

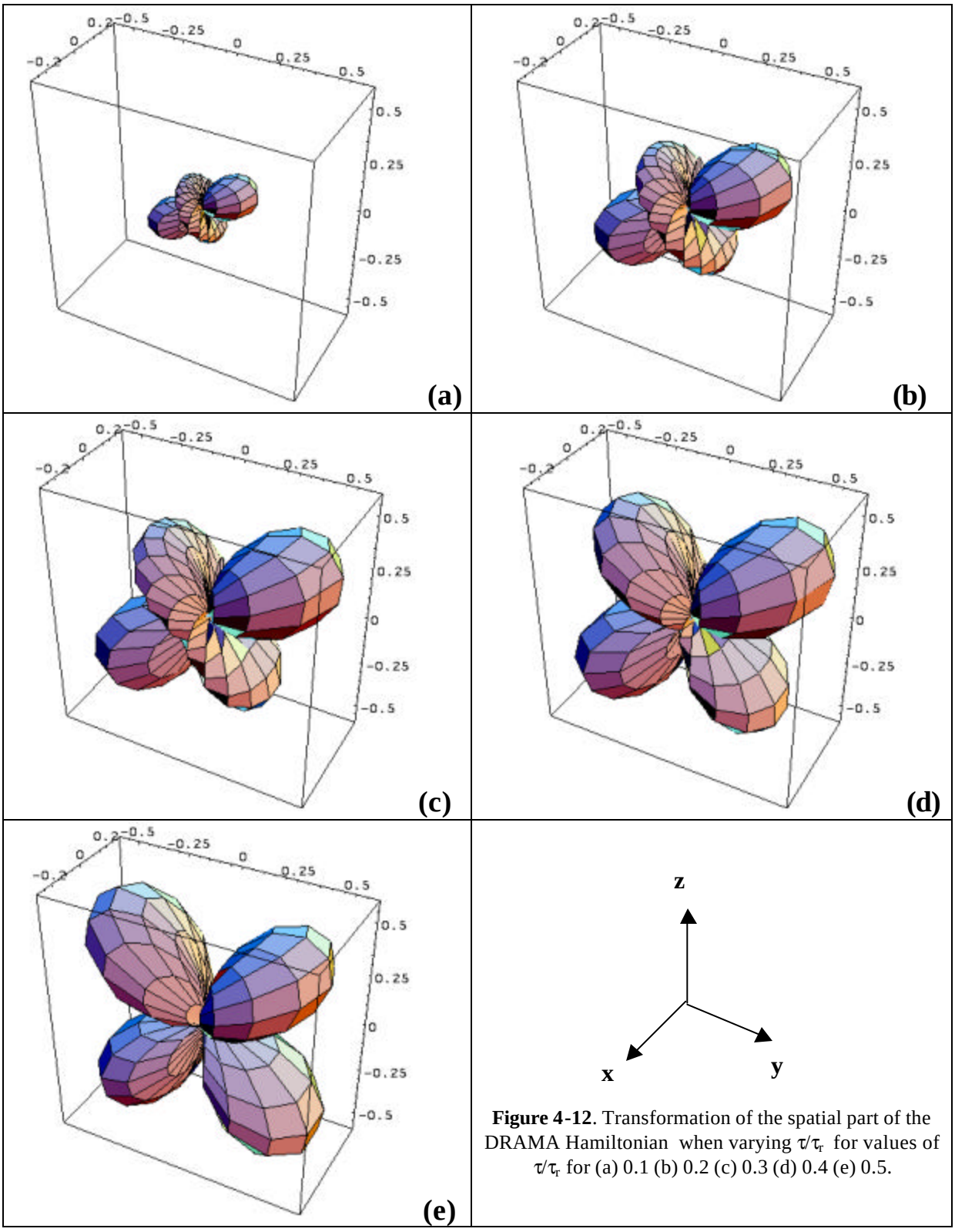

Figure 4-12. Transformation of the spatial part of the DRAMA Hamiltonian when varying τ/τ_r for values of τ/τ_r for (a) 0.1 (b) 0.2 (c) 0.3 (d) 0.4 (e) 0.5.

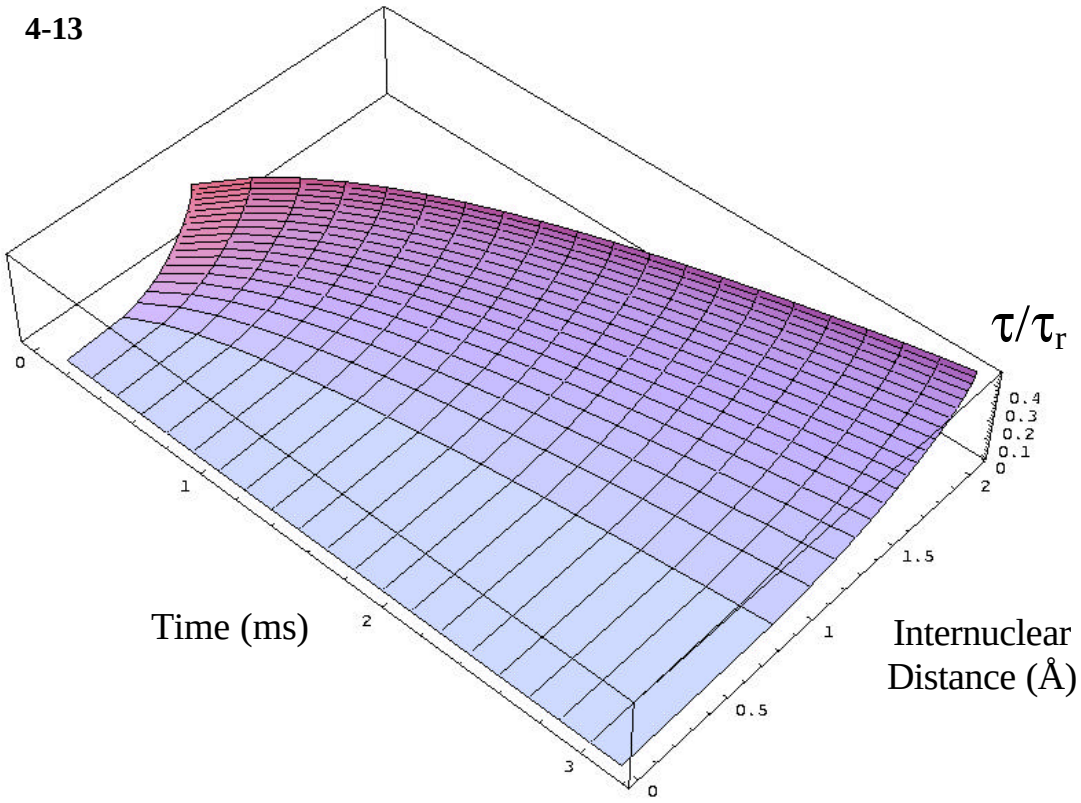

Figure 4-13: An implicit graph of the maximum coherence transfer (first maximum >50%) in a DRAMA pulse sequence, for internuclear distance and the ratio of τ/τ_r as a function of experimental time. The implicit maximum trends between 52% and 63% of normalized magnetization, which is correlated to the value of τ/τ_r..

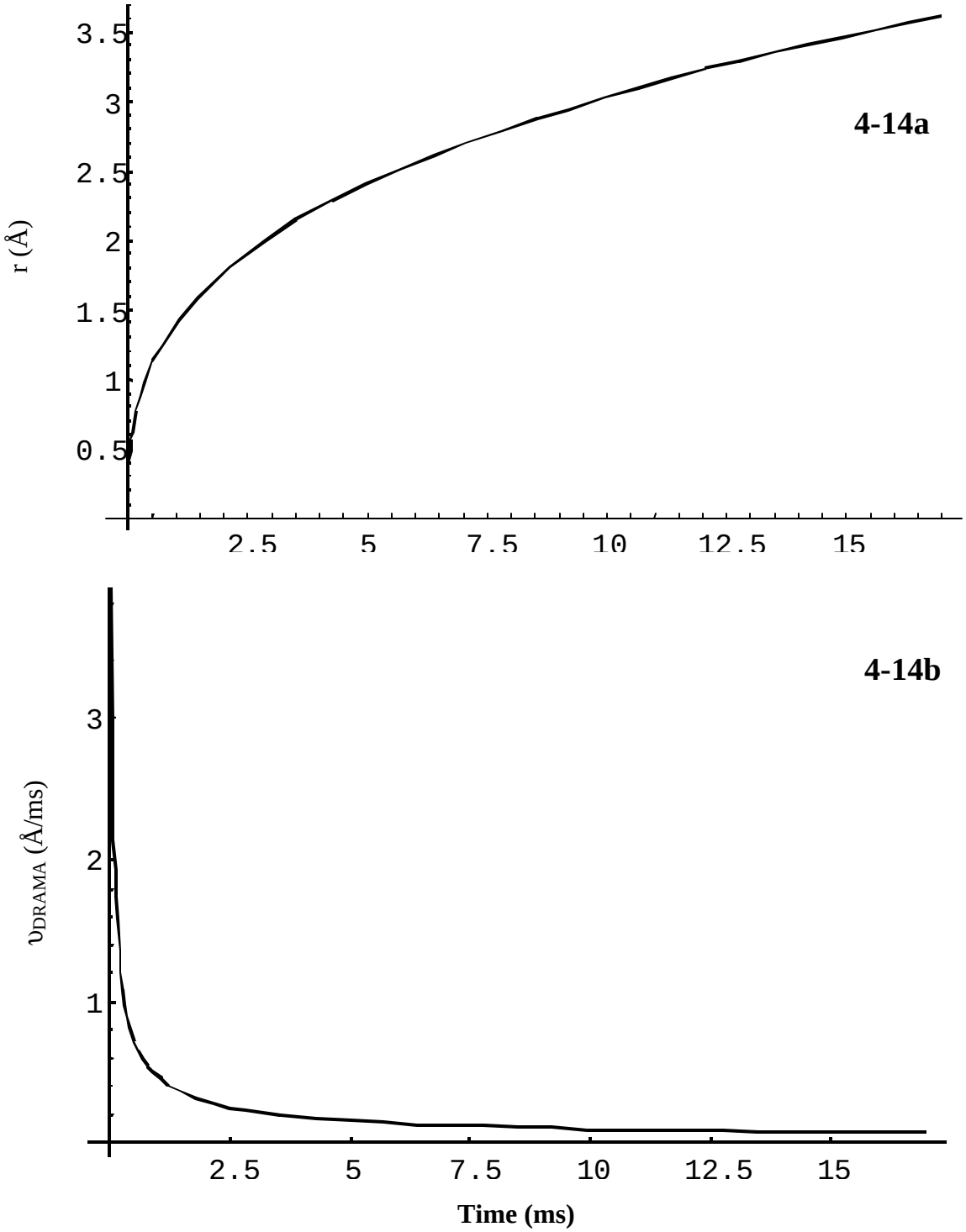

Figure 4-14: (a) The trace of maximum coherence diffusion peak ($r = 1.41\ t^{1/3}$) of Function B in Table 4-2, representing the maximum transferred transverse magnetization to the second spin in a DRAMA experiment as a function of experimental time where $\tau/\tau_r = 0.5$, for example when $\sigma(0) = I_x$. (b) The rate of coherence transfer, υ_{DRAMA}, versus experimental time (Å/ms). $\upsilon_{DRAMA} = 0.47\ t^{-2/3}$

The DRAWS Experiment

The DRAWS [57] average Hamiltonian, which arises from the recoupling pulse sequence in Figure 4-15, is an extension of the full dipolar Hamiltonian, with an additional zero-quantum operator term:

$$\tilde{\tilde{H}}_{DRAWS} = \frac{d}{17p}\left[c_{xx-yy}\left(I_x S_x - I_y S_y\right) + c_{zz}\left(3I_z S_z - \mathbf{I}\cdot\mathbf{S}\right)\right] \quad (4\text{-}7)$$

and spatial coefficients $c_{xx\text{-}yy}$ and c_{zz}

$$\begin{aligned} c_{xx-yy} = {} & -9.0468 \cos q \sin q \left[\sin\left(j + {}^{8p}/_{17}\right) + \cos\left(j + {}^{p}/_{34}\right)\right] \\ & + 4.8484 \sin^2 q \left[\sin\left(2j + {}^{p}/_{17}\right) + \cos\left(2j + {}^{15p}/_{34}\right)\right] \end{aligned} \quad (4\text{-}8a)$$

$$\begin{aligned} c_{zz} = {} & 9.0468 \cos q \sin q \left[\sin\left(j + {}^{8p}/_{17}\right) + \cos\left(j + {}^{p}/_{34}\right)\right] \\ & + 1.6161 \sin^2 q \left[\sin\left(2j + {}^{p}/_{17}\right) + \cos\left(2j + {}^{15p}/_{34}\right)\right] \end{aligned} \quad (4\text{-}8b)$$

whose two terms apiece are alternate trigonometric forms of the spherical harmonics Y_{lm} (as can easily be seen in Figure 4-16). The first term in both $c_{xx\text{-}yy}$ and c_{zz} which, like the spatial coefficients of DRAMA, are a result of the recoupled dipolar interaction and as shown in Chapter 2, are second-order-tensor components that contribute to the particular behavior of this Hamiltonian under powder averaging in Figure 4-17.

The plots in Figure 4-16 show the evolution of the DCT coefficients in Table 4-3 under the DRAWS average Hamiltonian in Eq. 4-7 as a function of DRAWS irradiation time. Curves A, B, C and D in Figure 4-16(a) represent expectation values of magnetization as functions of DRAWS irradiation times. Curve A, representing the expectation value of the Ix self-magnetization, actually has some appreciable magnetization change as the self-magnetization seems to lose coherence.

Because of the spin-lock conditions in the pulse sequence (along X) during free evolution (Figure 4-15), the DCT under the average Hamiltonian is primarily along the Y-axis. In Figure 4-15(b), curves E and F are indicative of the DCT coefficients along

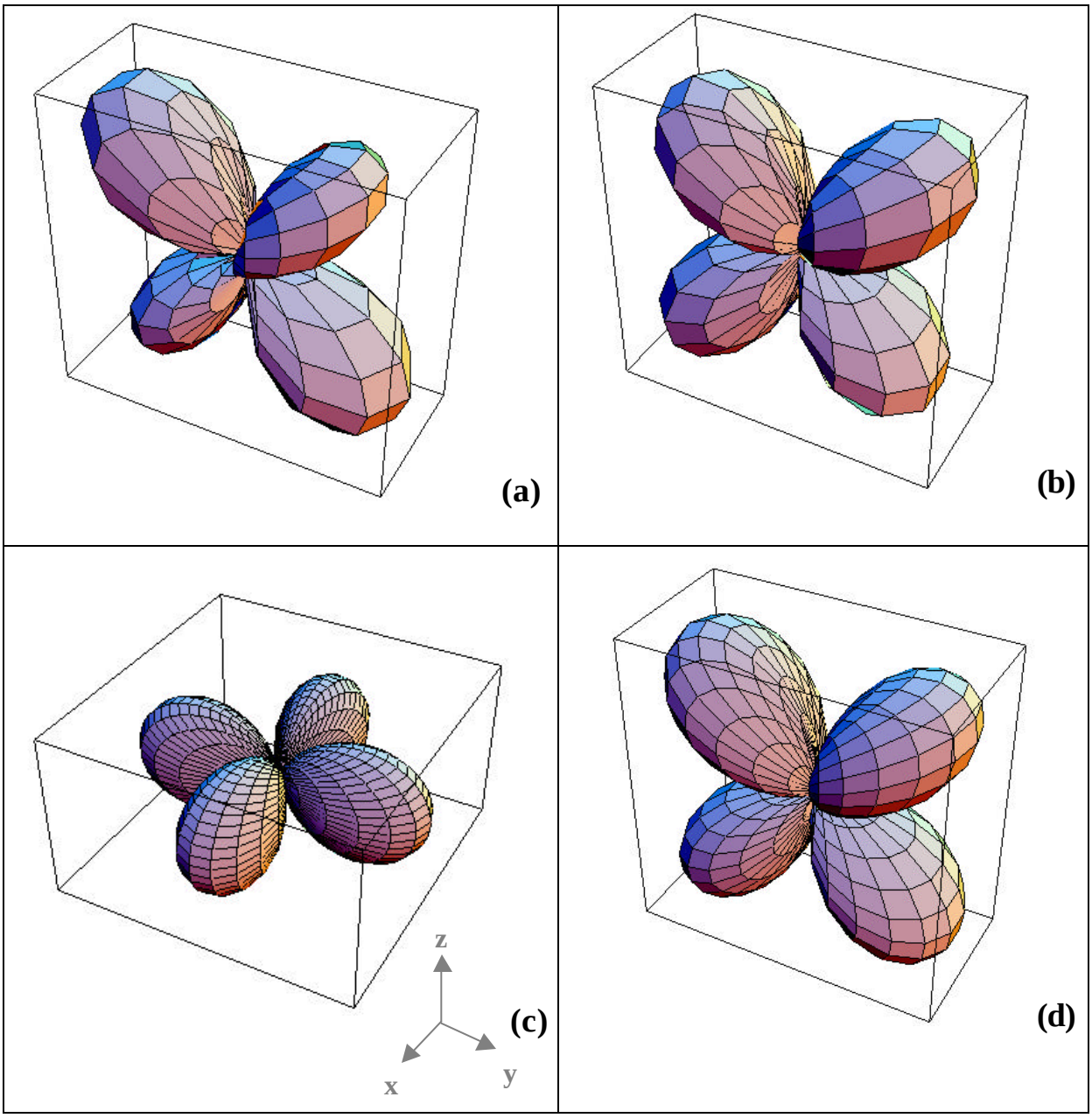

Figure 4-15: The spatial component of the DRAWS Hamiltonian. (all normalized) (a) the c_{xx-yy} term, showing the mix of yz and x^2-y^2 forms in the coefficient. (b) the c_{zz} term, which is dominated by the yz term rather than the x^2-y^2 term. (c) the x^2-y^2 term and (d) the yz terms directly from the c-coefficients of DRAWS.

Table 4-3: (this and next page): (a) Expectation values of operators evolving under the DRAWS coupling Hamiltonian. The initial states are given down the leftmost column. The evolving states are to be read across the row. For instance, Ix evolves to AIx + BSx – CIySz + DizSy.

s (0) ↓	**Ix**	**Sx**	**Iy**	**Sy**	**Iz**	**Sz**	**2IxSy**	**2IySx**	**2IxSz**	**2IzSx**	**2IySz**	**2IzSy**
Ix	A	B									- C	D
Sx	B	A									D	- C
Iy			E	F					G	- H		
Sy			F	E					- H	G		
Iz					J	K	- M	L				
Sz					K	J	L	- M				
2IxSy					M	-L	J	K				
2IySx					- L	M	K	J				
2IxSz			- G	H					E	F		
2IzSx			H	- G					F	E		
2IySz	C	- D									A	B
2IzSy	- D	C									B	A

(4-3a)

Table 4-3(b) Coefficients of the spin operators generated due to the evolution under H_{DRAWS}. $\alpha = 2c_{zz}$, $\beta = c_{xx} - c_{zz}$, $\gamma = -(c_{xx} + c_{zz})$

Function		Function	
A	$0.5\,(\cos(0.5(\alpha+\gamma)) + \cos(0.5(\alpha-\gamma)))$	**G**	$0.5\,(\sin(0.5(\alpha+\beta)) + \sin(0.5(\alpha-\beta)))$
B	$0.5\,(-\cos(0.5(\alpha+\gamma)) + \cos(0.5(\alpha-\gamma)))$	**H**	$0.5\,(\sin(0.5(\alpha+\beta)) - \sin(0.5(\alpha-\beta)))$
C	$0.5\,(\sin(0.5(\alpha+\gamma)) + \sin(0.5(\alpha-\gamma)))$	**J**	$0.5\,(\cos(0.5(\beta+\gamma)) + \cos(0.5(\beta-\gamma)))$
D	$0.5\,(\sin(0.5(\alpha+\gamma)) - \sin(0.5(\alpha-\gamma)))$	**K**	$0.5\,(-\cos(0.5(\beta+\gamma)) + \cos(0.5(\beta-\gamma)))$
E	$0.5\,(\cos(0.5(\alpha+\beta)) + \cos(0.5(\alpha-\beta)))$	**L**	$0.5\,(\sin(0.5(\beta+\gamma)) + \sin(0.5(\beta-\gamma)))$
F	$0.5\,(-\cos(0.5(\alpha+\beta)) + \cos(0.5(\alpha-\beta)))$	**M**	$0.5\,(\sin(0.5(\beta+\gamma)) - \sin(0.5(\beta-\gamma)))$

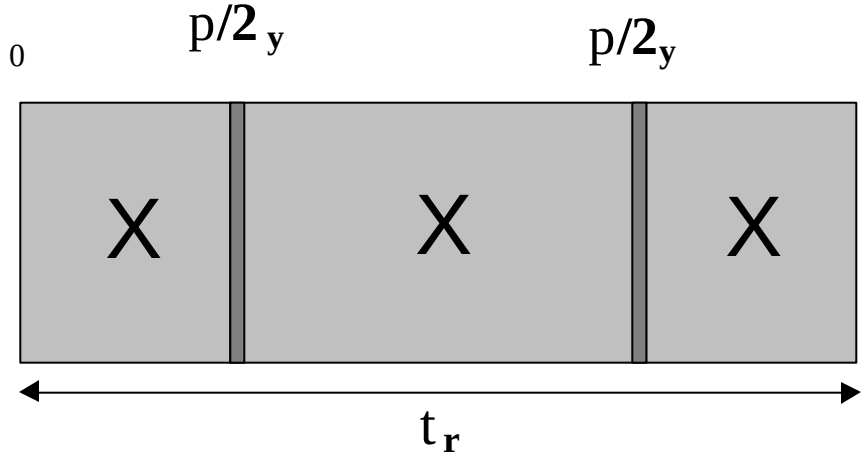

Figure 4-16: The DRAWS pulse sequence, with continuous rf irradiation applied between two $\pi/2_y$ pulses.

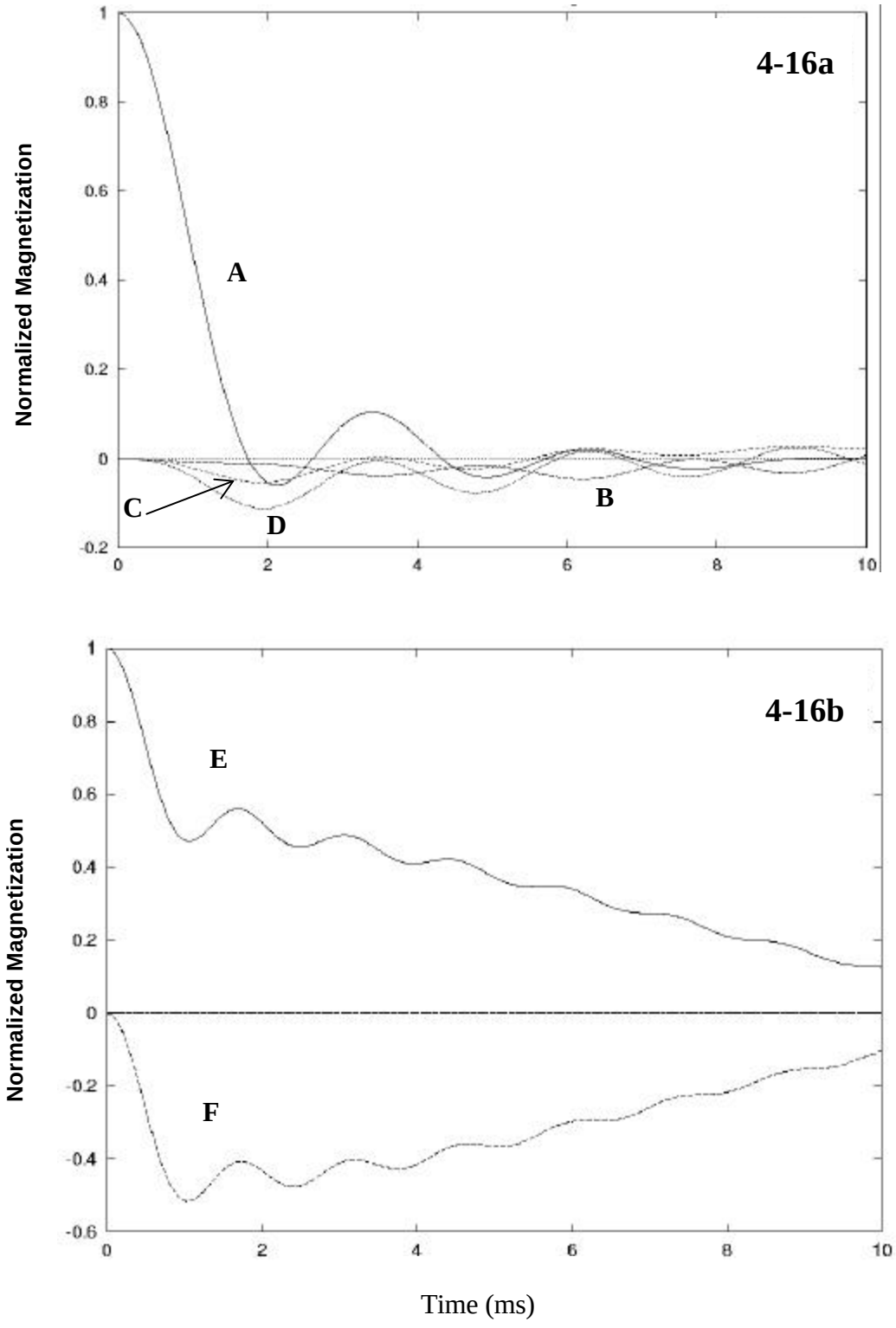

Figure 4-17: DRAWS coherence transfer coefficients from Table 4-3 for a ^{13}C homonuclear system as a function of DRAWS experimental time. r_{IS}=1.53Å. (a) A, B, C and D. (b) E, F.

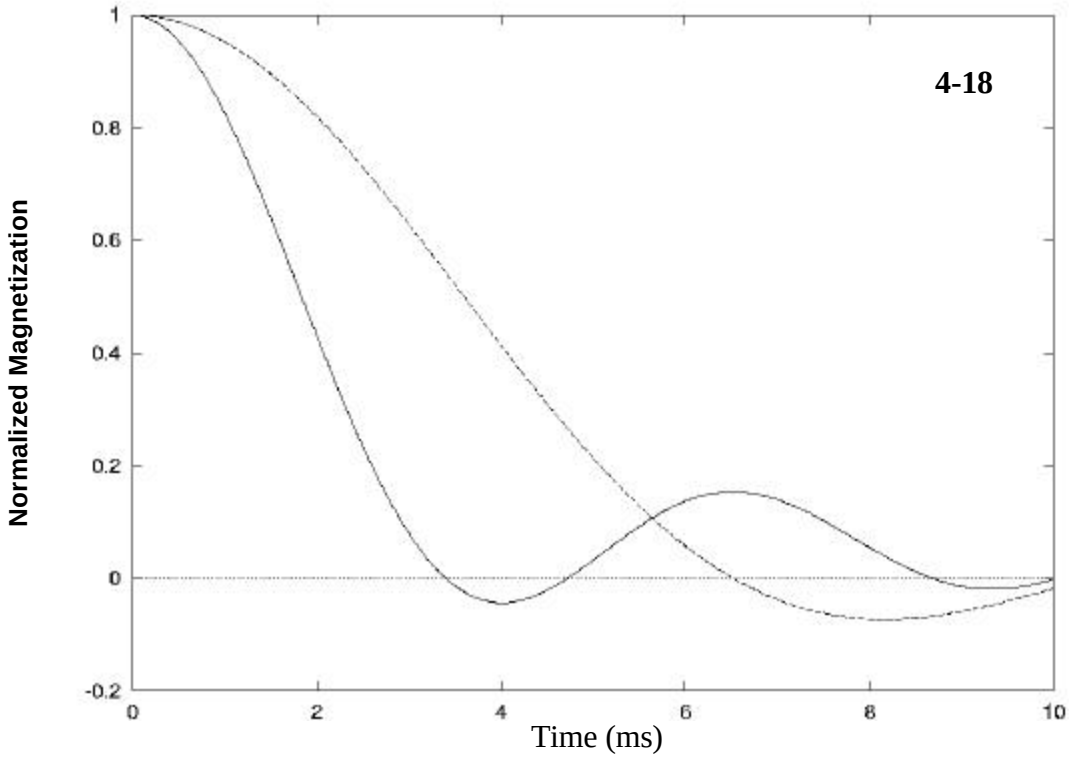

Figure 4-18: The powder-averaged expectation value <Iy+Sy> (solid line) corresponding to the sum of DCT coefficients E+F, and <Ix+Sx> (dotted line) corresponding to the sum of DCT coefficients A+B, plotted as a function of DRAWS irradiation time. Note the internuclear distance for both traces is r_{IS} = 2.39 Å, for purposes of comparison to reference [57].

the DCT operator pairs Iy and Sy. The coherence transfer has a typical rise-time for a MASDR experiment. Curve F exhibits a negative phase while curve E slowly loses phase over ten milliseconds. The strange appearance of the curves is supported by experiment. Not all DCT occurs through the Y-expectation values in the DRAWS experiment. Figure 4-18 shows the sum of the coherence transfer functions corresponding to the expectation values of <Iy + Sy> and <Ix + Sx> in an unoriented sample. Figure 4-18 certainly has a more conventional appearance than the curve F in Figure 4-17(b), as least as to what is expected for the typical expectation values we have encountered thus far. Experimental traces in Gregory *et. al*. [57] are similar, indicating that this model is correct.

DCT with the DRAWS Hamiltonian results in a slightly greater rate of coherence transfer than the transverse DCT in DRAMA, but still much less than the longitudinal transfer in an unoriented sample. Figure 4-19 gives the coherence transfer trace for

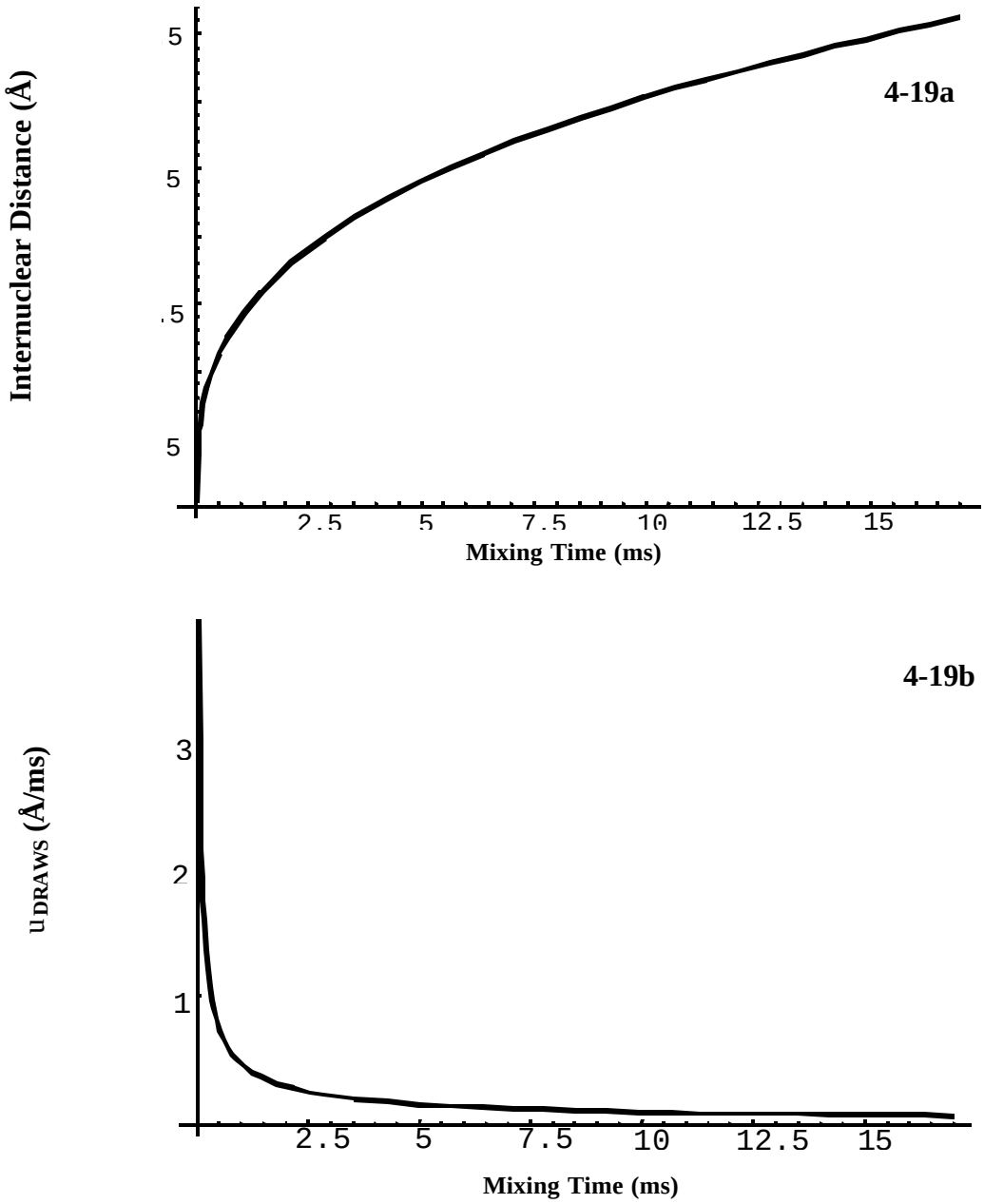

Figure 4-19: (a) The trace of the maximum coherence diffusion peak ($r = 1.51\ t^{1/3}$) of Function F in Table 4-2, as a function of DRAWS irradiation (mixing) time, representing the maximum transferred transverse magnetization to the second spin in a DRAWS experiment, for example when $\sigma(0) = Iy$. (b) The rate of coherence transfer, υ_{DRAWS} as a function of experimental time (Å/ms). $\upsilon_{DRAWS} = 0.503\ t^{-2/3}$

Eq. F in Table 4-3 following the "minimum" coherence transfer peak for the DCT to the second spin, which corresponds to the maximum peak in Eq. E. The plot was made with data from the program "pdraws.f" (Appendix A). The coherence transfer plot in Figure 4-19(a) corresponds to a DCT transfer equation of $r = 1.51\ t^{1/3}$. The rate of DRAWS DCT in 4-18(b) corresponds to $\upsilon_{DRAWS} = 0.503\ t^{-2/3}$, which is 56% of the full dipolar powder-averaged Hamiltonian in Figure 4-8(b). However, since the DRAWS experimental scaling is 0.33 compared to the powder-averaged dipolar Hamiltonian [57], this relatively high rate of coherence transfer as a function of DRAWS irradiation time is tempered by a low scaling factor.

The RFDR Experiment

The RFDR experiment [126], an improvement on the original SEDRA experiment and sometimes referred to as "longitudinal SEDRA," uses a compensated echo sequence of π pulses to induce a longitudinal mixing condition by creating a homonuclear dipolar flip-flop term through the difference in the isotropic chemical shift of two spins (Figure 4-20). The average Hamiltonian resulting from the combination of the chemical shift refocusing pulses and the dipolar interaction is

$$\tilde{\tilde{H}}_{RFDR} = d_{RFDR}\,(I_x S_x + I_y S_y)\,, \tag{4-9}$$

where, defining the rotor spinning frequency as ν_r, the isotropic chemical shift difference as $\Delta\delta$, and the Euler angles referencing the laboratory frame to the principal axis system as β and γ,

$$d_{RFDR} = \frac{2}{p}\sum_{m=1,2} d_{12,|m|}(b)\cos(mg)\frac{\Delta d/n_r}{m^2-(\Delta d/n_r)^2}(-1)^{m-1}\sin\left(p\,\frac{\Delta d}{n_r}\right) \tag{4-10}$$

where the term

$$d_{12,|m|}(b) = \frac{g_{IS}{}^2 \hbar}{r^3} d^2_{m0}(b) \qquad (4\text{-}11)$$

originates from the maximum possible dipolar coupling frequency and the Wigner rotation matrices $d^j_{mn}(\theta)$ [60]. The sum for $d_{12,|m|}(\beta)$ over m=1, 2 with cos(mγ) yields two terms, each describing forms of the spherical harmonics $Y_2{}^m$ in the RFDR average Hamiltonian. The RFDR Hamiltonian (Eq. 4-10) does not contain the IzSz generator, which restricts RFDR to primary longitudinal DCT, as discussed in Chapter 2. However, the powder-averaged dipolar recoupling term in RFDR is rather efficient, with the maximum-peak velocity υ_{RFDR} value of 0.61 (Figure 4-23) that is 68% of that of the pure dipolar Hamiltonian.

The index m in the sum of Eq. 4-10 signifies the two forms of the spherical harmonics while the ratio $\Delta\delta/\nu_r$ controls how much of either harmonic is expressed in the final form of d_{RFDR}. Figure 4-21 shows the magnitude (frequency) contribution of each term to the value of d_{RFDR} as a function of $\nu_r/\Delta\delta$ for the typical C_α-C_O peptide backbone distance of r_{IS}=1.53Å. Figure 4-23(a) and (b) exhibit the different resonant maxima for each harmonic term. The terms themselves have the same exact coherence transfer plots as a function of time when at their maxima…that is, when $\nu_r/\Delta\delta$ approaches1.0, the m=2 term nears zero (see Figure 4-21) while as the value of $\nu_r/\Delta\delta$ approaches 0.5, the m=1 term approaches zero. Powder-averaging over the entire form of d_{RFDR} when either term is near zero results in the same time-domain data, namely that of Figure 4-22(a), showing that powder averaging over the term at either maxima yields the same behavior. However, combinations of the two harmonic terms m=1 and m=2 results in an uneven distribution, as can be seen in Figure 4-22(c), whose time-evolution is shown in 4-21(b). The unevenness of the time-domain data results from the non-isotropic appearance of the frequency distribution in 4-22(c), where the lobes of the second-order tensor are distorted. Another interesting effect is that the coherence transfer term E, corresponding

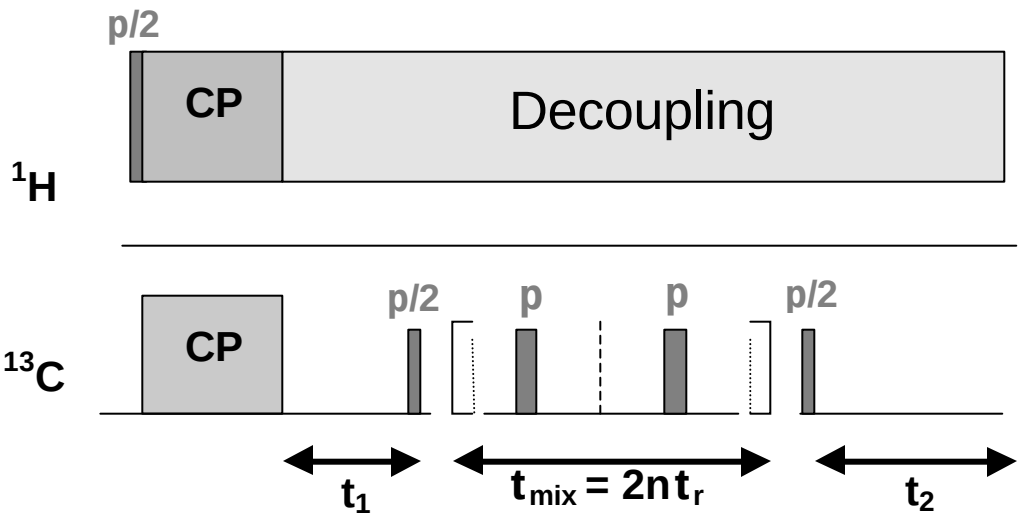

Figure 4-20: The RFDR pulse sequence. The phase of the πpulses are alternated in experiment over the period n..

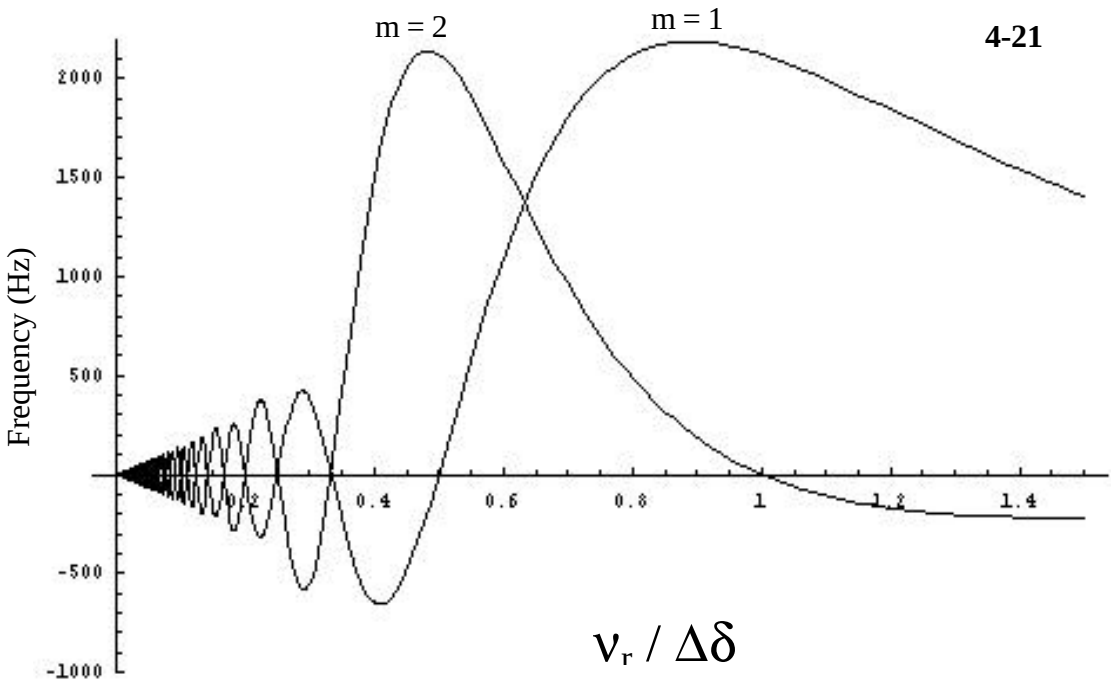

Figure 4-21: Effective coupling dRFDR vs. the dimensionless parameter of νr / Δδ for two model crystallite orientations (Eq.4-10). For the m=1 curve, d2,|1|(β)= 2153 Hz and d2,|2|(β)= 0Hz, and for the m=2 curve, d2,|1|(β)= 0 Hz and d2,|2|(β)= 2153 Hz. γ = 0 in both cases.

Table 4-4: (this and next page): **(a)** Expectation values of operators evolving under the RFDR coupling Hamiltonian. The initial states are given down the leftmost column. The evolving states are to be read across the row. For instance, Ix evolves to AIx + BIzSy.

s **(0)** ↓	**Ix**	**Sx**	**Iy**	**Sy**	**Iz**	**Sz**	**2IxSy**	**2IySx**	**2IxSz**	**2IzSx**	**2IySz**	**2IzSy**
Ix	A											B
Sx		A									B	
Iy			A							-B		
Sy				A					-B			
Iz					C	D	-E	E				
Sz					D	C	E	-E				
2IxSy					E	-E	C	D				
2IySx					-E	E	D	C				
2IxSz				B					A			
2IzSx			B							A		
2IySz		-B									A	
2IzSy	-B											A

Table 4-4(b): Coefficients of the spin operators generated due to the evolution under H_{RFDR} (Table 4-4(a))

Function	
A	cos(0.5at)
B	sin(0.5at)
C	$\cos^2(0.5at)$
D	$\sin^2(0.5at)$
E	0.5sin(at)

$a = d_{RFDR}$

to one half of the self-canceling zero-order coupling terms, reappears with the anisotropy caused by the combination of the two terms. It is absent in Figure 4-21(a) and may be a mathematical indicator of the amount of anisotropy depending on the ratio $\nu_r/\Delta\delta$ in the RFDR Hamiltonian.

RFDR's primary spin transfer mechanism, realized through the difference in the chemical shift between the two sites of interest, suffers from a susceptibility to T_2-type processes. For example, a symmetric distortion of the apparent static magnetic field that introduces a spread of the difference in the chemical shift, $\Delta\delta$, will certainly introduce a spread of apparent dipolar frequencies in RFDR. However, a spatially *symmetric* spread will manifest within the powder-averaged d_{RFDR} as an additional integral, acting as a weighting that should not significantly change the nature of the dipolar interaction. In Figure 4-23 (f), a calculation for the spatial part of the Hamiltonian using just such an integral spread is shown, normalized for the magnitude of the normal dipolar coupling constant d_{IS}. Because the static field gradient is symmetric across the distribution of frequencies in the sample, the second-degree-tensor nature of the interaction is unchanged, although the magnitude of the contribution of various frequencies has changed.

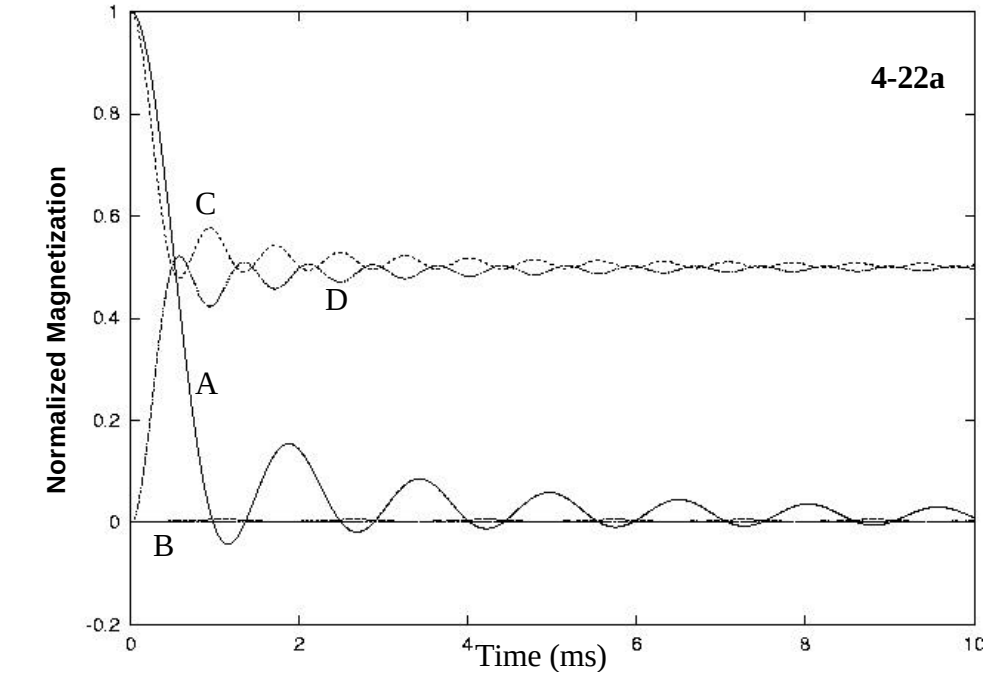

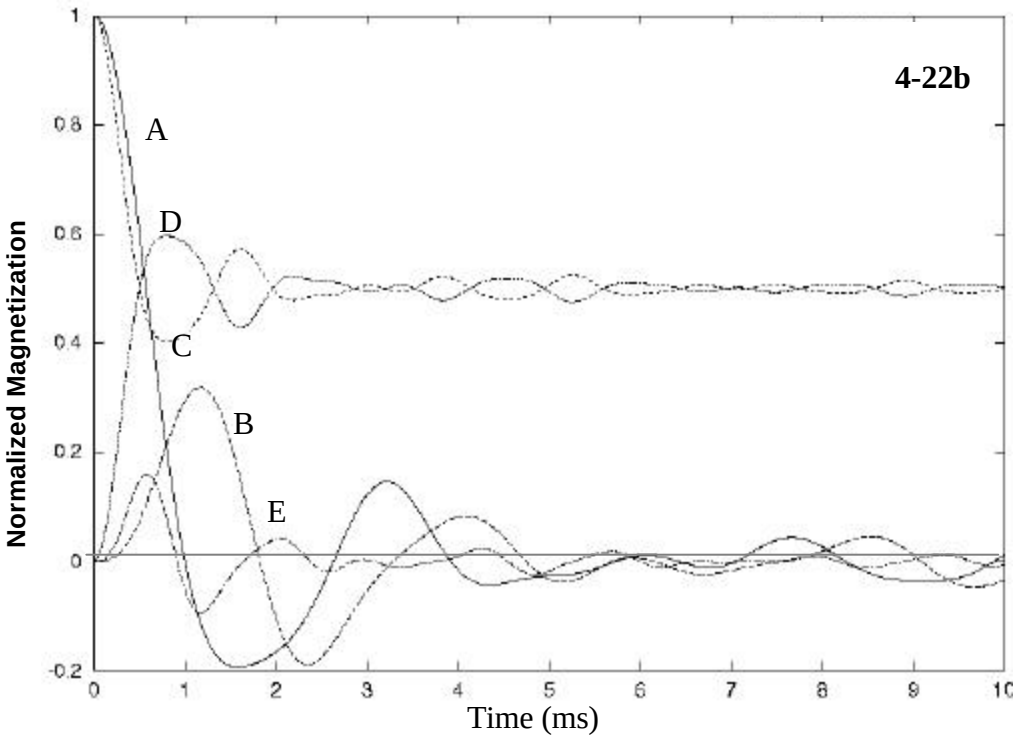

Figure 4-22: RFDR coherence transfer coefficients A, B, C and D. from Table 4-4 for a ^{13}C homonuclear system where r_{IS}=1.53Å. Plots are a function of RFDR experimental time. (a) With $\Delta\delta/\nu_r$ = 1.0, Note the coefficient B remains close to zero. (The coefficient E is approximately zero for all time in the powder average so does not appear here) (b) With $\Delta\delta/\nu_r$ = 1.5325, approximately where the two lines in Figure 4-21 have equal values.

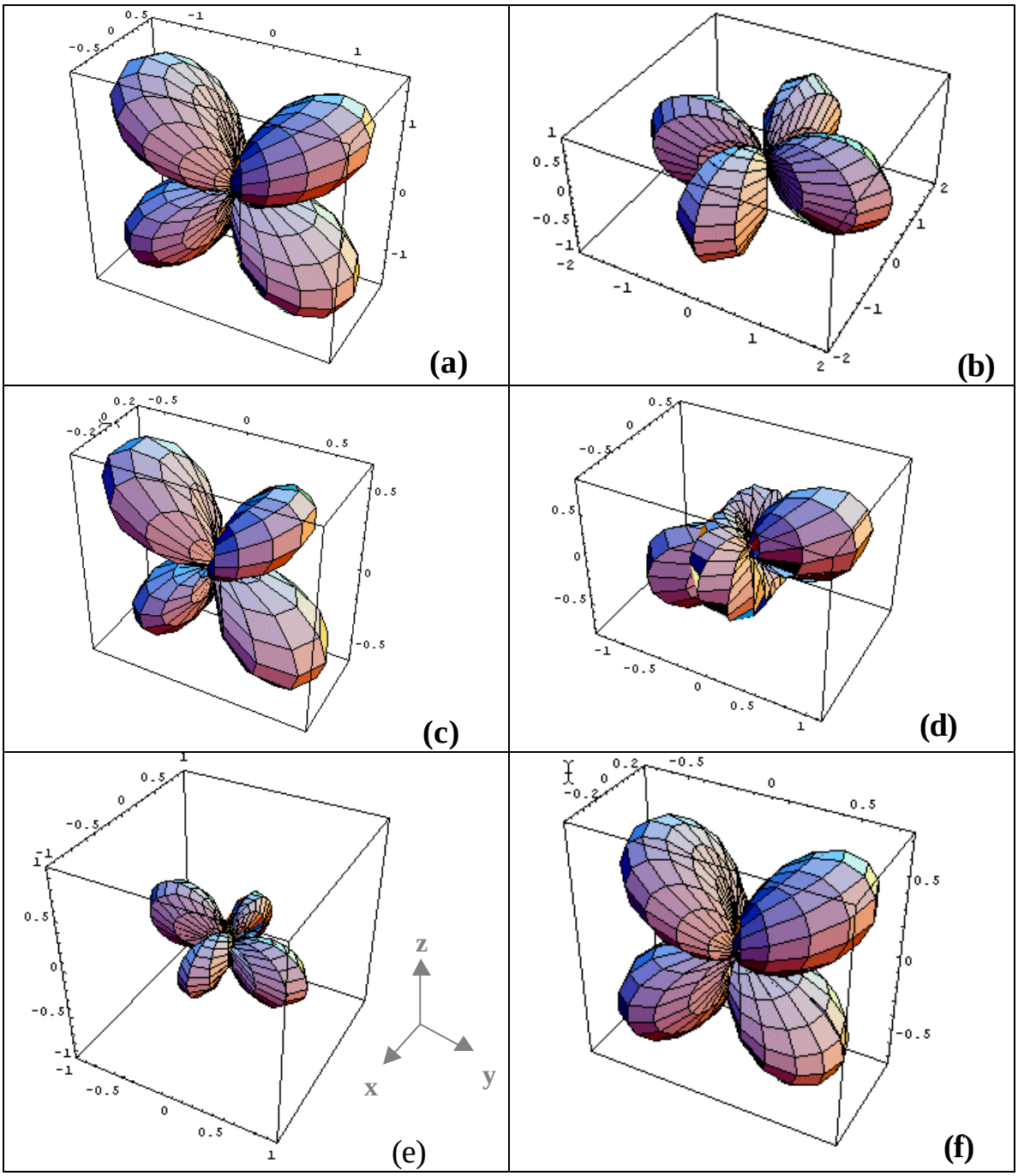

Figure 4-23: Parametric plots of the frequency distribution of dRFDR, normalized relative to the maximum dipolar coupling constant for the experiment. (a) $\Delta\delta/\nu r = 1.0$ (b) $\Delta\delta/\nu_r = 0.5$ (c) $\Delta\delta/\nu r = 1.5625$ (as in Figure 4-22(b). (d) $\Delta\delta = \Omega_I - \Omega_S = 123$ ppm, $\nu_r = 3.33$ kHz ($\Delta\delta/\nu r = 3.92$) ($\Delta\delta/\nu r = 1.86$) (e) $\Delta\delta/\nu_r = 2.61$, corresponding to $\nu r = 5.0$ kHz and $\Delta\delta = \Omega_I - \Omega_S = 123$ppm. (f) The same system as (e) but with a integral spread ranging over 1.2 ($\Omega_I - \Omega_S$), corresponding to a field inhomogeneity of 24.6 ppm.

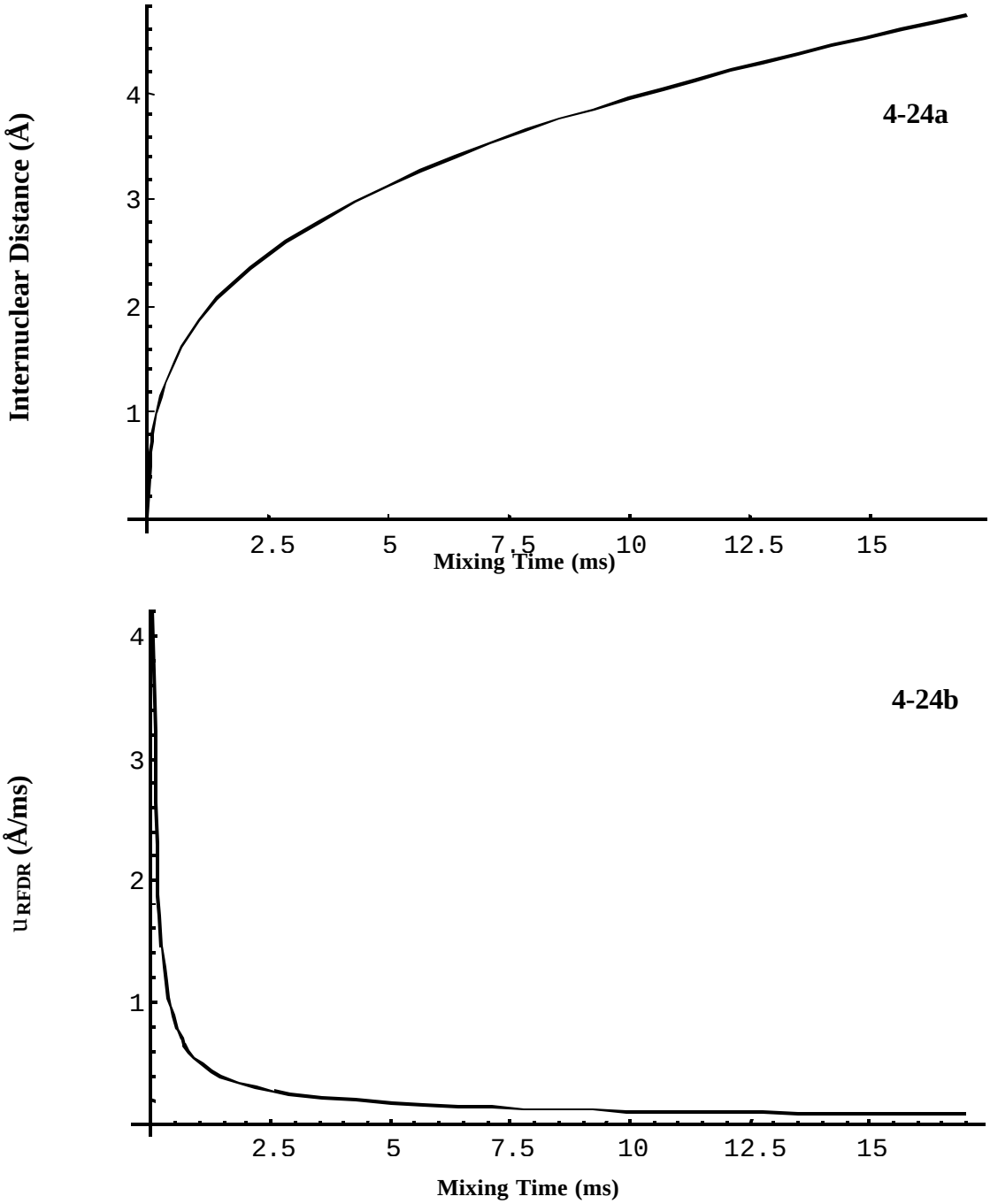

Figure 4-24: (a) The trace of maximum coherence diffusion peak ($r = 1.84\ t^{1/3}$) of Function D in Table 4-4, representing the maximum transferred transverse magnetization to the second spin in a RFDR experiment as a function of experimental time, for example when $\sigma(0) = Iz$. (b) The rate of coherence transfer, υ_{RFDR}, versus experimental time (Å/ms). $\upsilon_{RFDR} = 0.61\ t^{-2/3}$

The USEME Experiment

Thus far, each of the three experiments discussed (DRAMA, DRAWS, RFDR) have Hamiltonians that recoupled the dipolar interaction with an average Hamiltonian that differed from the full dipolar Hamiltonian in both spin and spatial components. USEME [58], however, recouples the dipolar interaction in a comparatively simple manner, with the full spin component of the dipolar Hamiltonian and a simple spatial component. USEME, as we will see, also has refocusing of chemical-shift offset "built in" to the experiment. What USEME lacks for complexity in the Hamiltonian it certainly returns to the experiment, as can be seen in Figure 4-25. USEME is a combination of spin-echo (to refocus the chemical shift) and magic-echo (to reestablish the dipolar interaction) sequences. The authors note that it recouples the dipolar interaction by 0.50.

Because of the simple form of the spatial part of the average Hamiltonian

$$\tilde{H}_{USEME} = \frac{3}{2p} S_1 (3IzSz - \mathbf{I} \cdot \mathbf{S}) \qquad (4\text{-}12)$$

calculation is straightforward. The term S_1 is as defined in references such as [60]

$$S_1 = D_{IS} \frac{3}{4} \sin 2q_m \sin 2q \sin j \qquad (4\text{-}13)$$

with D_{IS} defined in Equation 4-2, is one of the simplest spatial components in the dipolar-recoupling menagerie, and is visualized in Figure 4-26. Figure 4-27 shows the various forms of the coherence transfer functions for the USEME average Hamiltonian in Eq.(4-12) as a function of time. Although the spin part of Eq. 4-12 is identical to the full secular dipolar Hamiltonian, the particular properties of the spatial component in Eq. 4-13 renders functions E, F, and G zero under powder averaging. However, this is not detrimental whatsoever: it merely indicates that USEME does not share coherence between transverse and antiphase terms as occurs in the full dipolar Hamiltonian.

Analysis of the rate of USEME's coherence transfer, as established by the movement of the expected maximum through a distance r_{IS} as a function of experimental time, is shown in Figure 4-28. Fits to this curve establish the equation $r_{IS} = 1.51\ t^{1/3}$ with

an R-factor of 1. Therefore, USEME has approximately the same coherence transfer rate as DRAWS despite the different Hamiltonians for the two experiments, though USEME follows the coherence transfer behavior of a standard unoriented sample. Compare, for instance, functions C and D of USEME , Figure 4-27, with an unoriented sample in Figs. 4-1(c) and (d) and functions E and F of DRAWS in Fig. 4-17(b).

Table 4-5: (this and next page): (a) Expectation values of operators evolving under the USEME coupling Hamiltonian. The initial states are given down the leftmost column. The evolving states are to be read across the row. For instance, Ix evolves to AIx + BSx – EIySz + FIzSy.

s **(0)** ↓	**Ix**	**Sx**	**Iy**	**Sy**	**Iz**	**Sz**	**2IxSy**	**2IySx**	**2IxSz**	**2IzSx**	**2IySz**	**2IzSy**
Ix	A	B									-E	F
Sx	B	A									F	-E
Iy			A	B					E	-F		
Sy			B	A					-F	E		
Iz					C	D	-G	G				
Sz					D	C	G	-G				
2IxSy					G	-G	C	D				
2IySx					-G	G	D	C				
2IxSz			-E	F					A	B		
2IzSx			F	-E					B	A		
2IySz	E	-F									A	B
2IzSy	-F	E									B	A

Table 4-5(b): Coefficients of the spin operators generated due to the evolution under H_{USEME}

Function	
A	$0.5(\cos(\alpha\pi t)+\cos(\beta\pi t))$
B	$0.5(-\cos(0.5(\alpha\pi t)+\cos(\beta\pi t)$
C	$0.5(1+\cos(\gamma\pi t))$
D	$0.5(1-\cos(\gamma\pi t))$
E	$0.5(\sin(\alpha\pi t)+\sin(\beta\pi t))$
F	$0.5(\sin(\alpha\pi t)-\sin(\beta\pi t))$
G	$0.5(\sin(\gamma\pi t))$

$\alpha=0.5S_1$ $\beta=0.5S_1$ $\gamma=S_1$, (S_1 defined in Eq. 4-13)

Figure 4-25: The USEME pulse sequence. The spin-echo (SE) sequence refocuses the chemical shift, while the magic echo (ME) recouples the dipolar interaction.

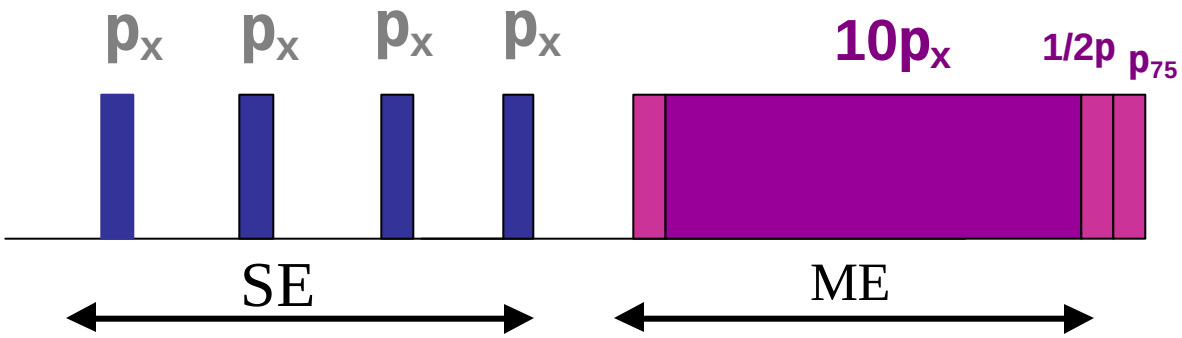

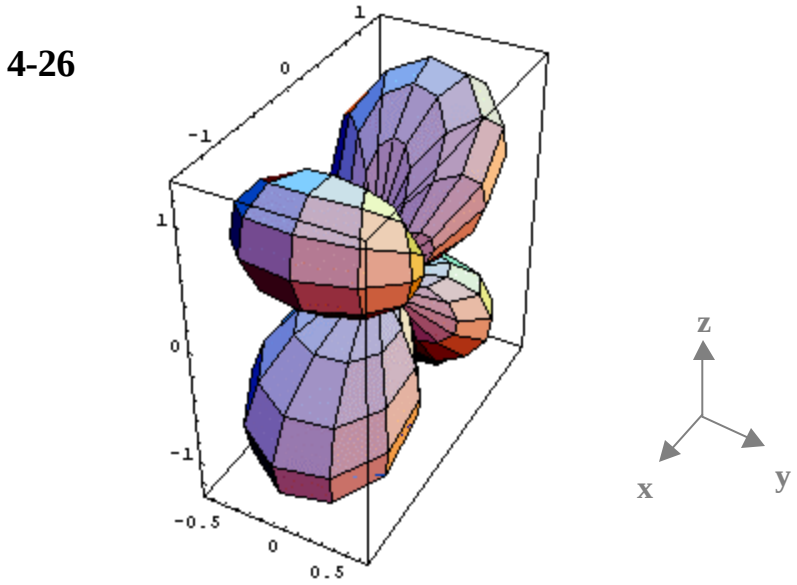

Figure 4-26: Parametric plot of the frequency distribution of d_{USEME}, normalized relative to the maximum dipolar coupling constant for the experiment.

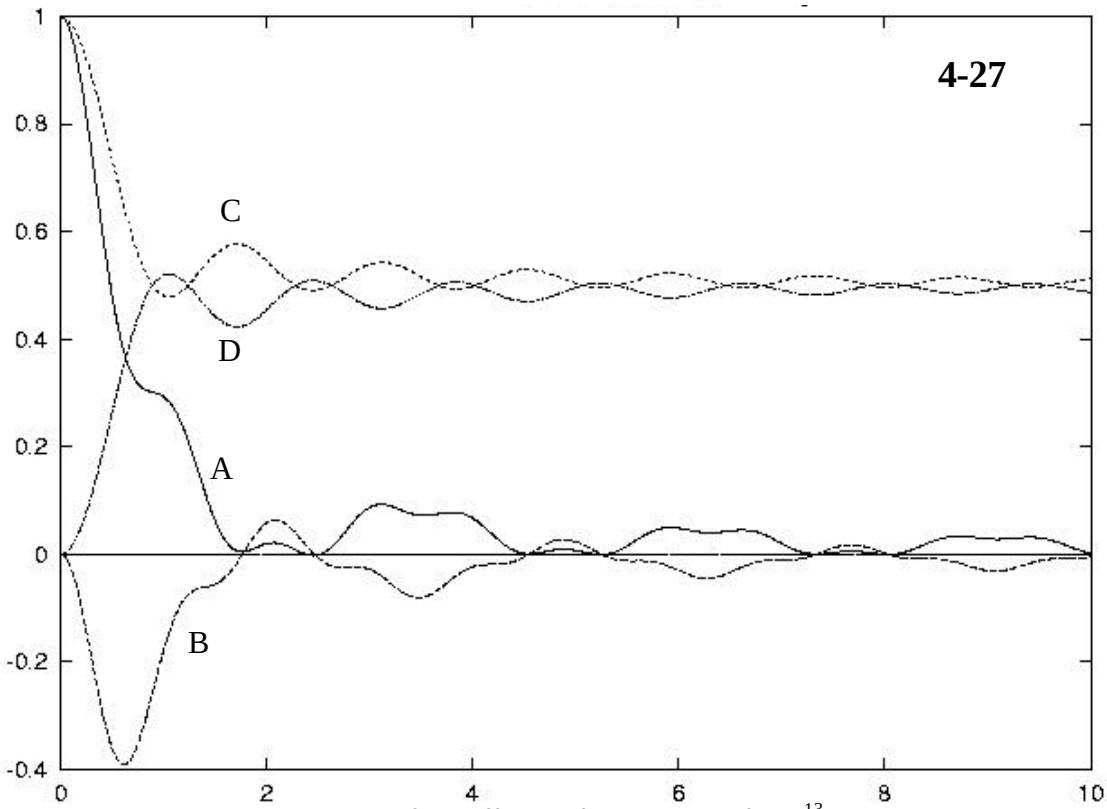

Figure 4-27: USEME coherence transfer coefficients from Table 4-4 for a ^{13}C homonuclear system as a function of USEME experimental time. r_{IS}=1.53Å for the coefficients A, B, C ,D. The coefficients E, F, and G are approximately zero for all time in the powder average so do not appear in this graph

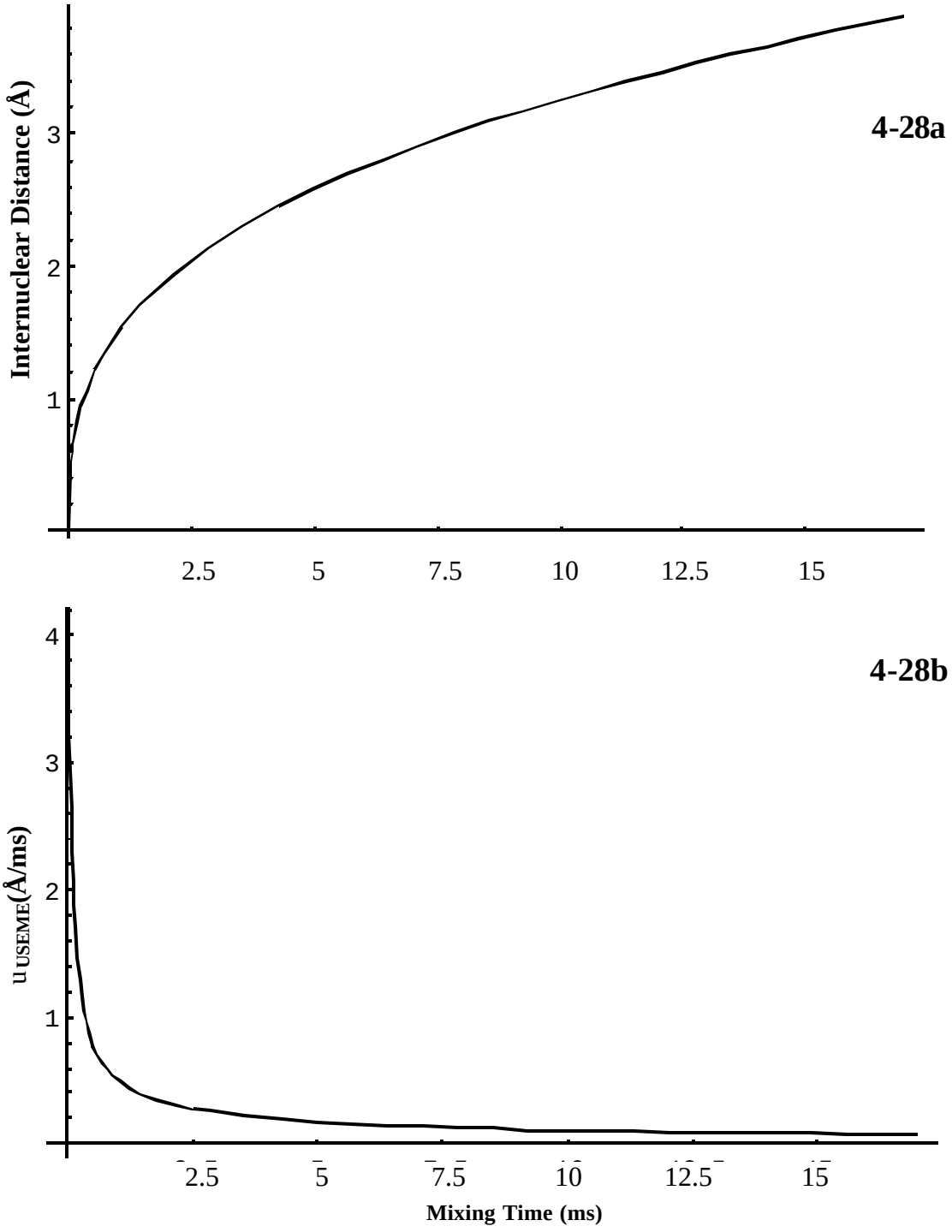

Figure 4-28: (a) The trace of maximum coherence diffusion peak (r =1.51 t $^{1/3}$) of Function D in Table 4-5, representing the maximum transferred transverse magnetization to the second spin in a USEME experiment as a function of experimental time, for example when $\sigma(0) = Iz$. (b) The rate of coherence transfer, υ_{USEME}, versus experimental time (Å/ms). $\upsilon_{USEME} = 0.50\ t^{-2/3}$

Conclusions

As we have shown, dipolar coherence transfer can differ between recoupling experiments. The DCT of several experiments on unoriented samples have been analyzed, and now the coherence transfer characteristics of each experiment can be compared. Figure 4-29 presents the various experiments' coherence transfer rates for comparison. However, before we reach conclusions on the efficacy of any experiment based on its coherence transfer rate, rise time, and susceptibility to relaxation processes, we should first revisit the goals of coherence transfer study: namely, to gather information on the internuclear distances in hard-to-measure samples that may have more than one (isolated) coherence transfer pair.

Depending on the information needed from a multi-labeled system, either a rapid or slow coherence transfer rate may be desired. A slow DCT rate could be useful for an experiment goal that attempts to approximate a system of distantly coupled pairs in terms of isolated pairs rather than groups. Further exploration of that idea should be reserved for first-order approximation studies for various geometries of multi-spin systems. It might be found that, to first approximation, a pair in a diffuse multi-spin group with slow DCT could be found to be successfully approximated as an isolated pair for short experimental times. However, that conjecture aside, the experiment with the slowest coherence transfer rate, DRAMA, is also the experiment which is most susceptible to T_2-relaxation processes, which would become more pronounced as the mixing time increases under less-than-ideal experimental conditions.

Assuming that every experimental coherence transfer pair can be said to be isolated (for instance in a suitably labeled protein), a rapid coherence transfer rate such as found in RFDR would reduce the effects of relaxation by reducing experimental time.

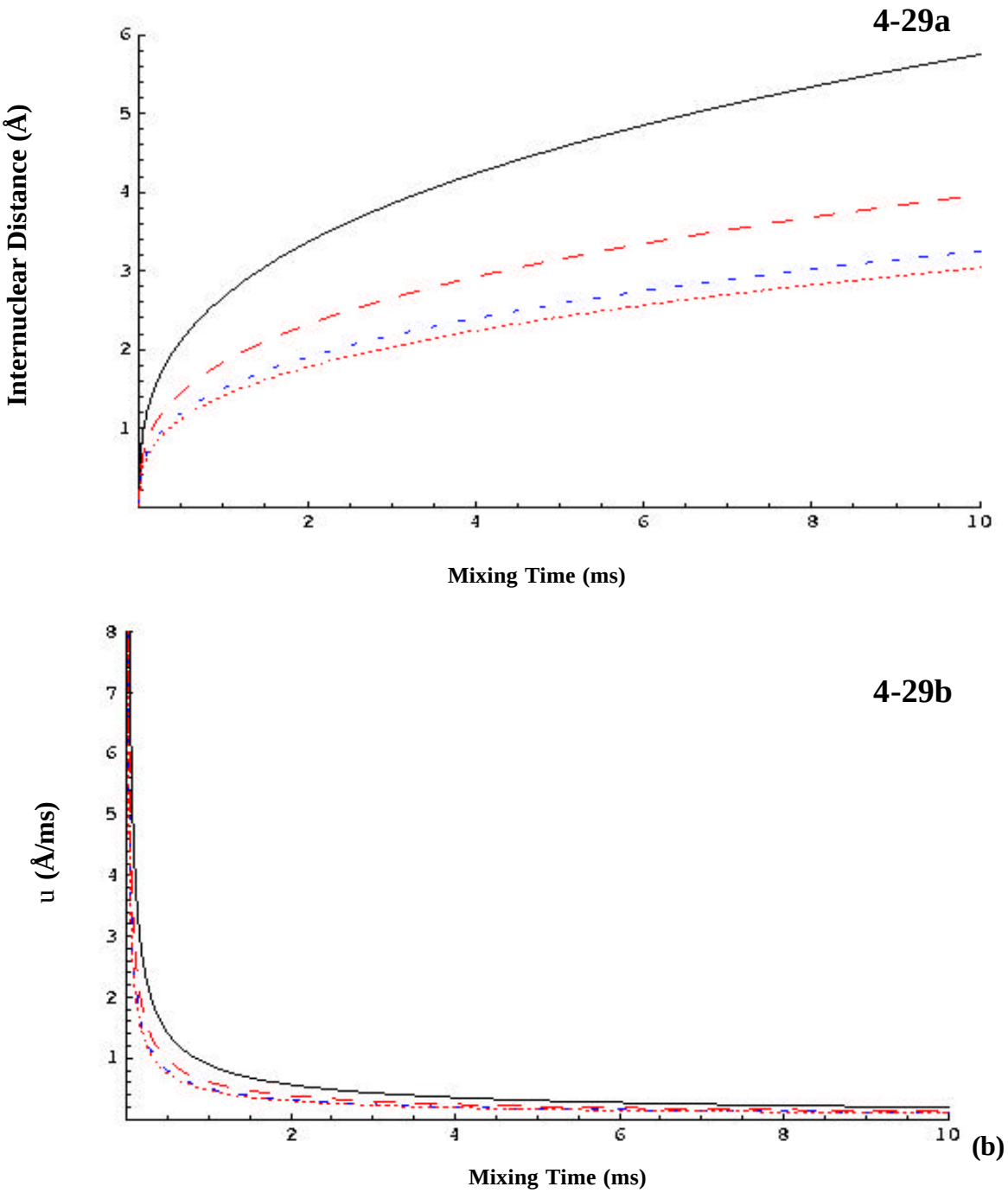

Figure 4-29: Coherence transfer compared for all MASDR experiments over 10 ms. Solid line: unoriented sample. Long-dashed line: RFDR. Short dashed line: USEME and DRAWS. Dense dotted line: DRAMA. (a) The trace of maximum coherence diffusion for several dipolar-recoupling experiments. (b) The instantaneous velocity of dipolar coherence transfer, υ, for the same range of mixing times.

4-30

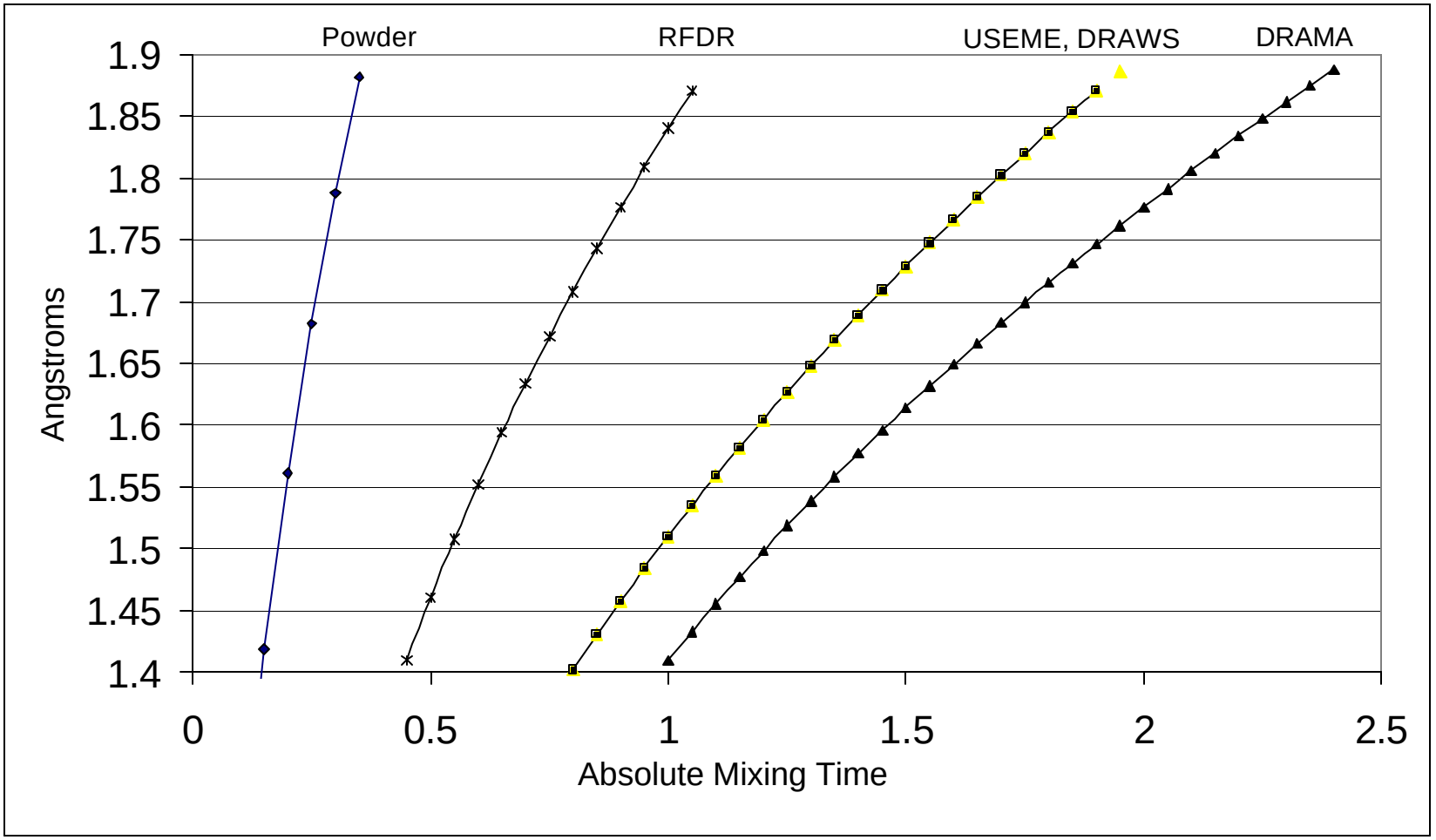

Figure 4-30: Distance of maximum DCT peak as a function of experimental mixing time over a range of distances relevant to peptide backbone $^{13}C_{\alpha}$ - $^{13}C_{O}$ experiments. Data key is labeled above each series. For DRAMA, $\Delta\delta/\nu_r$=0.5; for RFDR, m=1. USEME and DRAWS are essentially identical.

However, a rapid transfer of coherence across a set of sample pairs reduces the ability to resolve the different pairs given small differences in their internuclear distances. To compare the coherence transfer across a range of distances important for, example, peptide backbone studies ($^{13}C_{\alpha}$ - $^{13}C_{O}$) Figure 4-30 gives the coherence transfer rates over a range of relevant distances (1.40 to 1.85Å) for comparison.

Table 4-6: Summary of position and velocity coefficients for maximum-peak DCT for several recoupling experiments as compared to the static unoriented powder sample

Experiment	**X, $r = X t^{1/3}$**	**V, $u = V t^{-2/3}$**
Static powder	2.67	0.89
RFDR	1.84	0.61
DRAWS	1.51	0.50
USEME	1.51	0.50
DRAMA	1.41	0.47

It can be noted immediately that DRAMA, with its ability to selectively target specific distances and mixing times via the ratio of $\Delta\delta/\nu_r$ (see Figure 4-11) may be an ideal basis for further refinement to target specific spin-pair internuclear distances. The relatively slow coherence transfer rate over the range in Figure 4-30 makes it the most ideal MASDR experiment for resolving different spin pairs in experimental time. Additionally, the "fine tuning" aspect of DRAMA, with further development and attention to reduction of chemical shift offsets, may prove valuable in selecting out specific isolated spin-pairs in experiment.

Given the information at hand, what is the final analysis? It may come down to a condition of a "happy medium" supposing all experimental conditions are equally sensitive. DRAMA has the strength of fine-tuning and slow coherence transfer rate, but

its weakness lies in its susceptibility to transverse relaxation processes, as it transfers magnetization through Iy.

RFDR has a rapid coherence transfer rate, but also depends on the chemical shift offset to provide the conditions for MASDR; a spread in chemical shift offsets would increase the dipolar coherence transfer as well as cause a loss of resolution in the experiment. Additionally, it is also susceptible to transverse relaxation processes.

DRAWS has a complex Hamiltonian and experimental structure. It transfers magnetization in a spin-lock state and therefore may be especially susceptible to sample anisotropies.

USEME may very well be the “happy medium,” with a coherence transfer rate between RFDR and DRAMA, and equal to that of DRAWS. USEME has, built-in, a chemical-shift refocusing element that may make it less susceptible than DRAMA or RFDR to dephasing by T_2 processes; additionally, USEME transfers magnetization longitudinally using a Hamiltonian that is one of the simplest in the MASDR menagerie. In comparison, DRAMA's loss of phase due to T_2 processes during CT may render it a more difficult experiment to perform, while faster CT processes may make targeting of maximum CT difficult. Therefore, some kind of experimental design using supercycling of USEME experiments during specific times appropriate for maximum coherence transfer among a range of peptide bond distances may be a first step in determining the utility of such a strategy.